



저작자표시-비영리-변경금지 2.0 대한민국

이용자는 아래의 조건을 따르는 경우에 한하여 자유롭게

- 이 저작물을 복제, 배포, 전송, 전시, 공연 및 방송할 수 있습니다.

다음과 같은 조건을 따라야 합니다:



저작자표시. 귀하는 원저작자를 표시하여야 합니다.



비영리. 귀하는 이 저작물을 영리 목적으로 이용할 수 없습니다.



변경금지. 귀하는 이 저작물을 개작, 변형 또는 가공할 수 없습니다.

- 귀하는, 이 저작물의 재이용이나 배포의 경우, 이 저작물에 적용된 이용허락조건을 명확하게 나타내어야 합니다.
- 저작권자로부터 별도의 허가를 받으면 이러한 조건들은 적용되지 않습니다.

저작권법에 따른 이용자의 권리는 위의 내용에 의하여 영향을 받지 않습니다.

이것은 [이용허락규약\(Legal Code\)](#)을 이해하기 쉽게 요약한 것입니다.

[Disclaimer](#)

공학석사 학위논문

**Study on Exceptional Point of
Non-Hermitian Chiral Plasmonic
Nanomaterials**

비-허미시안 카이럴 플라즈모닉 나노물질의
특이점에 대한 연구

2021년 8월

서울대학교 대학원

재료공학부

임 예 찬

**Study on Exceptional Point of Non-Hermitian
Chiral Plasmonic Nanomaterials**

지도 교수 남 기 태

이 논문을 공학석사 학위논문으로 제출함

2021년 8월

서울대학교 대학원

재료공학부

임 예 찬

임예찬의 석사 학위논문을 인준함

2021년 8월

위 원 장 김 미 영

부위원장 남 기 태

위 원 유 선 규

Abstract

Study on Exceptional Point of Non-Hermitian Chiral Plasmonic Nanomaterials

Yae-Chan Lim

Department of Materials Science and Engineering

The Graduate School

Seoul National University

Discovery of parity-time symmetry (PT -symmetry) has made a huge impact on non-Hermitian physics. It not only redefined the concept of quantization in quantum dynamics, but expanded the scope of the mathematical physics from real to complex analysis. Also, the PT -symmetric non-Hermitian concept can be applied in photonics due to the similarity of the Schrödinger equation and Maxwell's equation. Most of the time, the application of non-Hermitian physics to photonics is achieved by two coupled system with gain and loss. Two coupled system makes a Hamiltonian of 2×2 matrix, and its eigenvalues are found to be square roots of a complex quantity, which forms a Riemann surface in complex plane.

The introduction of non-Hermitian physics to photonics brought out numerous applications utilizing its topology and singularity. For example, a recent research reported asymmetric mode switching depending on the propagation direction of light. Furthermore, the concept of non-Hermiticity has

been realized even in plasmonics, and it provided a novel approach for ultrasensitive molecular sensing. Park and coworkers demonstrated the symmetry-breaking-induced exceptional points in plasmonic system through the fabrication of coupled nanorods array. They modulated near-field and far-field coupling by controlling the displacement along x-axis between the coupled rods and the periodicity along y-axis. The mode interference of two hybridized plasmon modes produced two topologically intertwined modes which coincide at the exceptional point. They also compared the sensitivity of the fabricated EP sensor with the conventional DP sensors, and reported a record sensitivity of 4,821 nm per RIU.

Based on the lessons gained from non-Hermitian Plasmonics, we focused on the extension of the understanding of non-Hermitian physics to chiral plasmonics. Chiral Plasmonic nanomaterials possess spin-dependent optical properties which can be modulated by the handedness of circular polarization of light. These chiroptical properties have facilitated a variety of optical applications utilizing chiral phenomena. While a lot of applications have been realized by the top-down fabrication, Lee and coworkers reported the solution-based synthesis method of chiral plasmonic nanoparticle fabrication. The synthesized chiral nanoparticles possess strong optical activity via the mixing of electric and magnetic dipole in their gap structure. Therefore, the implementation of the non-Hermiticity to the chiral nanoparticle arrays is believed to make a significant impact in the field of chiral plasmonics.

However, the complex optical properties have inhibited the rigorous analysis of the nanoparticles, so the simplified description of the chiral nanoparticle is required. Born-Kuhn model is the simplest model describing chiral materials by using two orthogonally coupled oscillators. In order to understand the interrelationship between non-Hermiticity and chiral plasmonic

nanomaterials, it is important to establish the fundamental theoretical background. In that sense, Born-Kuhn model can be a useful tool to explore in more detail as its dimension is easily modulated. Therefore, our research has focused on the demonstration of the exceptional point of Born-Kuhn by theoretical and numerical procedures.

For the theoretical approach, coupled mode theory (CMT) has been utilized to describe the coupled plasmon modes. We adopted the mutual coupling constant to the regular dynamic equation of plasmon mode, and due to the chiral nature of the mutual coupling constant of the Born-Kuhn model, different exceptional points appear for LCP and RCP incidence.

Numerical demonstration has been successively conducted to corroborate the theoretical prediction. A finite element method (FEM) based Maxwell's equation solver, COMSOL, has been utilized during the procedure. The displacement and periodicity of the array structure of Born-Kuhn model were modulated, and S-parameters were obtained under LCP and RCP incidence. In accordance with the theoretical prediction, the exceptional point changed its location according to the LCP and RCP incidence.

This result indicates the potential application for ultrasensitive chiral molecule sensing. According to the perturbation theory regarding the exceptional point, the mode shift is proportional to the square root of the perturbation. Thus, if we assume that the system is located at the exceptional point for LCP incidence but not for RCP incidence, the system is more sensitive for LCP. As chiral sensitivity is defined as the difference of the mode shifts for LCP and RCP, the Born-Kuhn model can amplify the chiral sensitivity so that it can be utilized for an ultrasensitive chiral molecule sensor.

In conclusion, this thesis focused on the fundamental understanding of

the role of chiral nanomaterials in non-Hermitian photonics. In addition, the theoretical description of the non-Hermiticity of chiral plasmonic resonators has been accomplished. Furthermore, the demonstration of spin-controlled EP diagram implies the potential application for ultrasensitive biomolecule sensing.

Keywords: Non-Hermitian physics, PT-symmetry, Exceptional point, Chiral plasmonics, Coupled mode theory

Student Number: 2019-24094

Contents

Chapter 1. Introduction	1
1.1 Non-Hermitian Physics	1
1.2 Non-Hermitian Photonics	5
1.3 Non-Hermitian Approach for Plasmonics	11
1.4 Bibliography	17
Chapter 2. Chiral Plasmonics.....	20
2.1 Chirality and Chiral Plasmonics	20
2.2 Fabrication of Chiral Nanostructures	23
2.3 The Simplest Chiral Model: Born-Kuhn Model.....	26
2.4 Extended Born-Kuhn Models	28
2.5 Objective of Thesis	33
2.6 Bibliography	34
Chapter 3. Non-Hermitian Approach for Born-Kuhn Model	37
3.1 Coupled Mode Theory	37
3.2 Theoretical Demonstration of the Exceptional Point	39
3.3 Numerical Demonstration of the Exceptional Point.....	45
3.4 Bibliography	51
Chapter 4. Concluding Remarks	52

List of Figures

Figure 1 Finding of PT -symmetry in non-Hermitian system results in the complex extension of quantum mechanics.....	4
Figure 2 (a) Two coupled system composed of gain and loss. (b) Real and imaginary part of the eigenmodes as a function of the gain and loss coefficient.....	9
Figure 3 Previous research of non-Hermitian photonics. (a) Asymmetric mode switching. (b) Negative refraction. (c) Orbital angular momentum micro-laser. (d) Optical-spin black hole.	10
Figure 4 (a) Schematic of coupled nanorods array. (b) Hybridization of the coupled plasmon modes. (c) Mode interference between bonding and anti-bonding mode.....	13
Figure 5 The resonance frequency (left) and loss rate (right) as a function of lateral shift d_x and the y-direction periodicity P_y	14
Figure 6 (a) EP Diagram of the resonance frequencies and loss rates. Real and imaginary part of the plasmon modes as a function of d_x (b) for $P_y = 400$ nm, (c) for $P_y = 430$ nm.....	15
Figure 7 (a) Comparison of mode shift between DP and EP sensor. (b) Mode shift as a function of perturbation for DP and EP sensor.....	16
Figure 8 Chiroptical responses of the constructed gold gammadion nanostructures, (a) CD spectra for left- and right-handed PCM. (b) Electric field and optical chirality distribution at III.	22

Figure 9 (a) Synthesis of chiral gold nanoparticles. (b) Calculated chiroptical distribution of the chiral nanoparticles ¹⁷	24
Figure 10 (a) Multipole analysis of the scattering cross-section of 432 helicoid III. Polarization current distribution (b) at 560 nm, (c) at 590 nm.	25
Figure 11 (a) Devised Born-Kuhn model for the description of chiral molecules. (b) Mode hybridization of Born-Kuhn model.	27
Figure 12 (a) Born-Kuhn model does not fully describe 3-dimensional chiral materials. (b) Optical properties of Born-Kuhn model are strongly dependent on the incidence direction.	28
Figure 13 (a) Implementation of the extended Born-Kuhn model. (b) Comparison of optical properties of Born-Kuhn model and the extended Born-Kuhn model.	31
Figure 14 (a) 432 symmetry of 432 helicoid III. (b) Construction of 432 Born-Kuhn model by the successive 3-fold, 4-fold, and 2-fold rotation.	32
Figure 15 (a) Schematic of the single plasmonic resonator in coupled mode theory and (b) its corresponding extinction spectrum	38
Figure 16 (a) Schematic of Born-Kuhn model described by the coupled mode theory. (b) Extinction spectrum which has spectral peaks at ω^- and ω^+	40
Figure 17 Diagrams for the real and imaginary part of the hybrid resonance frequencies $\tilde{\omega}^+$ and $\tilde{\omega}^-$ as a function of δ and κ	41
Figure 18 Optical simulation of the Born-Kuhn model. (a) Schematic showing	

the dimensions for the constructed Born-Kuhn model. (b) Calculated mutual coupling constants for left- and right-handed circular polarization.....	43
Figure 19 (a) Optical simulation of the parallelly coupled rods. (a) Schematic showing the dimensions for the constructed model of parallelly coupled rods. (b) Calculated mutual coupling constants for left- and right-handed circular polarization.	44
Figure 20 Optical simulation of the periodic Born-Kuhn model. (a) Schematic of the simulation setup. (b) Three-dimensional design for the periodic structure of the Born-Kuhn model. (c) The dimensions of the Born-Kuhn unit.....	46
Figure 21 Resonance frequencies and loss rates under the illumination of left-handed circular polarized light as a function of d_x for (a) $P_y = 490$ nm, (b) $P_y = 500$ nm and (c) $P_y = 510$ nm	48
Figure 22 EP diagrams of the resonance frequencies and loss rates for (a) left-handed and (b) right-handed circular polarization	49
Figure 23 (a) Different EP diagrams for LCP and RCP incidence. (b) Different mode shift as a function of perturbation for LCP (red) and RCP (blue)	50

Chapter 1. Introduction

1.1 Non-Hermitian Physics

In quantum physics (also in classical physics), Hamiltonian is used to describe the time evolution of a system. However, adequate boundary conditions are required for complete description, and depending on the boundary conditions, the system is determined whether *closed* or *open*.¹ A closed system is one that its boundary is not in contact with its environment, so the total probability of the system is preserved in time.

$$\frac{d}{dt} \int_{-\infty}^{\infty} P(x,t) dx = \frac{d}{dt} \int_{-\infty}^{\infty} |\Psi(x,t)|^2 dx = 0. \quad (1.1)$$

In conventional quantum physics, it is also called a Hermitian system because the Hamiltonian of the system is Hermitian, which means the Hamiltonian H is the same as its conjugate transpose H^\dagger . One of the most significant features of the Hermitian Hamiltonian is that its eigenvalues are always real. On the other hand, an open system (or non-Hermitian system) is one that is subject to the influence of its environment, so the total probability changes in time. The Hamiltonian of the open system is not Hermitian, which is $H \neq H^\dagger$, and its eigenvalues are not real in general. This is why people had not addressed non-Hermitian systems for a long time. However, Bender and Boettcher found that even a non-Hermitian Hamiltonian can have real eigenvalues if it has a symmetry under simultaneous parity and time-reversal operation, which is called “ PT -symmetry”.²

In order to evaluate the symmetry of a system, parity and time-reversal operation are used. The parity operation flips the sign of the spatial coordinates of the system, and the time-reversal operation reverses the time flow of the

system. The action of both parity and time-reversal operator on a wavefunction ψ gives,³

$$PT\psi = \lambda\psi. \quad (1.2)$$

Since the square of the combined parity and time-reversal operator is unit operator, $(PT)^2 = \mathbf{1}$, a multiplication of (1.2) by PT gives,

$$\begin{aligned} (PT)^2\psi &= (PT)(\lambda\psi) \\ \psi &= (PT)\lambda(PT)^2\psi \\ \psi &= (PT)\lambda(PT)(PT)\psi \\ \psi &= \lambda^* \lambda \psi = |\lambda|^2 \psi. \end{aligned} \quad (1.3)$$

Therefore, we obtain $|\lambda|^2 = 1$ where the eigenvalue is a pure phase, $\lambda = e^{i\alpha}$. The phase angle α can be chosen such that $\lambda = 1$. For a system described by a Hamiltonian having PT -symmetry, the following relation between the Hamiltonian and its PT -reflected one is required:

$$H^{PT} = (PT)H(PT)^{-1} = (PT)H(PT) = H. \quad (1.4)$$

Also, the PT operator commutes with the Hamiltonian:

$$(PT)H = H(PT). \quad (1.5)$$

If the PT -operator and the Hamiltonian share a common eigenfunction, the effect of the PT -operator on the Hamiltonian equation $H\psi = E\psi$ gives,

$$\begin{aligned}
(PT)H\psi &= (PT)E\psi \\
H(PT)\psi &= (PT)E(PT)(PT)\psi \\
H\psi &= E^*(PT)\psi \\
E\psi &= E^*\psi.
\end{aligned} \tag{1.6}$$

This confirms that the eigenvalue of PT -symmetric Hamiltonian is real, since it is equal to its complex conjugate, $E = E^*$.

A Hamiltonian is composed of kinetic and potential energy,

$$H = -\frac{\hbar^2}{2m}\nabla^2 + V(\mathbf{r}). \tag{1.7}$$

Each action of parity operator and time-reversal operator on the Hamiltonian gives,

$$\begin{aligned}
PHP &= -\frac{\hbar^2}{2m}\nabla^2 + V(-\mathbf{r}), \\
THT &= -\frac{\hbar^2}{2m}\nabla^2 + V^*(\mathbf{r}).
\end{aligned} \tag{1.8}$$

Thus, a combined parity and time-reversal operation reveals that

$$(PT)H(PT) = -\frac{\hbar^2}{2m}\nabla^2 + V^*(-\mathbf{r}). \tag{1.9}$$

This confirms that the condition for a Hamiltonian having PT -symmetry is $V(\mathbf{r}) = V^*(-\mathbf{r})$, which means the real part of the potential function should be even while the imaginary part should be odd.

The finding of PT -symmetric Hamiltonian has a significant implication since it expanded the mathematical description of physical theories from real to complex analysis.⁴ This complex generalization of the conventional quantum physics allows us to address the physical phenomena in complex domain and reappraise the conventional theories based on the Hermitian mechanics. One of the most remarkable case is the quantization of energy. Since Planck discovered the quantized energy states from the black-body radiation, it has been a long-held belief that all energy states are quantized. However, the extension of the parametric domain describing the energy states let us realize that the energy states are, in fact, intertwined with each other and the quantization of energy is just a projection on the real domain.

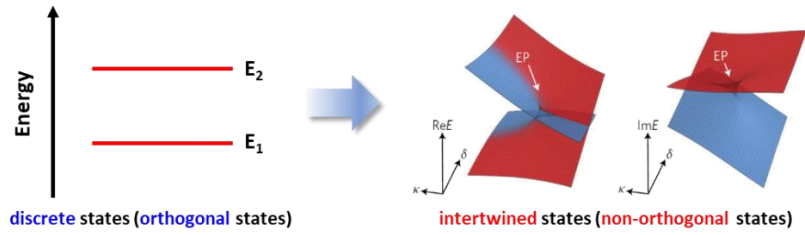


Figure 1 Finding of PT -symmetry in non-Hermitian system results in the complex extension of quantum mechanics.

1.2 Non-Hermitian Photonics

While the implementation of parity-time symmetry is conceptually striking, experimental verification in quantum systems still remains challenging due to the difficulty of the demonstration of PT -symmetry in non-Hermitian quantum mechanical systems. Thanks to the flexibility of photonics that can be controlled conveniently, the exploration of PT -symmetric non-Hermitian physics has found ground in photonics.⁵⁻⁷ Although the physical origins of the Schrodinger equation and Maxwell's equation is different, transforming an equation with some premises makes their mathematical structures similar.⁸

When we start with the four Maxwell's equations,

$$\begin{aligned}\nabla \cdot \mathbf{D} &= 0, \\ \nabla \cdot \mathbf{B} &= 0, \\ \nabla \times \mathbf{E} &= -\frac{\partial \mathbf{B}}{\partial t}, \\ \nabla \times \mathbf{H} &= \frac{\partial \mathbf{D}}{\partial t},\end{aligned}\tag{1.10}$$

and the constitutive relations of a non-magnetic medium give,

$$\begin{aligned}\mathbf{D} &= \epsilon(\mathbf{r})\epsilon_0\mathbf{E}, \\ \mathbf{B} &= \mu_0\mathbf{H},\end{aligned}\tag{1.11}$$

where $\epsilon(\mathbf{r})$ is the relative permittivity of the medium. If we use the vector identity,

$$\nabla \times \nabla \times \mathbf{A} = \nabla(\nabla \cdot \mathbf{A}) - \nabla^2 \mathbf{A},\tag{1.12}$$

the electric field has the following relation:

$$\nabla \times \nabla \times \mathbf{E} = \nabla(\nabla \cdot \mathbf{E}) - \nabla^2 \mathbf{E}. \quad (1.13)$$

A curl of 3rd equation in (1.10) gives,

$$\begin{aligned} \nabla \times \nabla \times \mathbf{E} &= \nabla \times \left(-\frac{\partial \mathbf{B}}{\partial t} \right) = -\frac{\partial}{\partial t} (\nabla \times \mathbf{B}) \\ &= -\mu_0 \frac{\partial}{\partial t} (\nabla \times \mathbf{H}) = -\mu_0 \frac{\partial^2 \mathbf{D}}{\partial t^2} \\ &= -\epsilon(\mathbf{r}) \epsilon_0 \mu_0 \frac{\partial^2 \mathbf{E}}{\partial t^2}. \end{aligned} \quad (1.14)$$

Also, inserting the 1st relation in (1.11) on the 1st equation in (1.10) gives,

$$\begin{aligned} \nabla \cdot \mathbf{D} &= \nabla \cdot (\epsilon(\mathbf{r}) \epsilon_0 \mathbf{E}) \\ &= \epsilon_0 (\mathbf{E} \cdot \nabla \epsilon(\mathbf{r}) + \epsilon(\mathbf{r}) \nabla \cdot \mathbf{E}) = 0, \end{aligned} \quad (1.15)$$

and

$$\nabla \cdot \mathbf{E} = -\mathbf{E} \cdot \frac{\nabla \epsilon(\mathbf{r})}{\epsilon(\mathbf{r})} = -\mathbf{E} \cdot \nabla (\log \epsilon(\mathbf{r})). \quad (1.16)$$

Thus, the first term on the right-hand side in (1.13) is:

$$\nabla(\nabla \cdot \mathbf{E}) = -\nabla(\mathbf{E} \cdot \nabla (\log \epsilon(\mathbf{r}))). \quad (1.17)$$

Inserting (1.14) and (1.17) on (1.13) gives a vector wave equation:

$$\nabla^2 \mathbf{E} - \epsilon(\mathbf{r}) \epsilon_0 \mu_0 \frac{\partial^2 \mathbf{E}}{\partial t^2} = -\nabla(\mathbf{E} \cdot \nabla (\log \epsilon(\mathbf{r}))) \quad (1.18)$$

For certain cases characterized by

$$\mathbf{E} \perp \nabla \epsilon(\mathbf{r}), \quad (1.19)$$

(1.18) becomes a Helmholtz equation:

$$(\nabla^2 - \epsilon(\mathbf{r})\epsilon_0\mu_0 \frac{\partial^2}{\partial t^2})\mathbf{E} = 0. \quad (1.20)$$

For simplicity, if we consider x-polarized light propagating the medium in z-direction, it becomes a scalar wave equation, and considering a monochromatic harmonic wave, $E(\mathbf{r}, t) = \tilde{E}(\mathbf{r})e^{-i\omega t}\hat{e}_x$, (1.20) changes into

$$(\nabla^2 + \epsilon(\mathbf{r})\frac{\omega^2}{c^2})\tilde{E} = 0. \quad (1.21)$$

The electric field propagating in z-direction is expressed by

$$\tilde{E}(\mathbf{r}) = \psi(\mathbf{r})e^{ik_0 n_0 z}, \quad (1.22)$$

where $\psi(\mathbf{r})$ is a wave amplitude and n_0 is bulk refractive index of the medium.

This changes (1.21) into

$$((\nabla + ik_0 n_0 \hat{e}_z)^2 + \epsilon(\mathbf{r})\frac{\omega^2}{c^2})\psi = 0 \quad (1.23)$$

In a stratified or cylindrical symmetric medium, the electric permittivity becomes a function of transverse coordinate, $\epsilon(\mathbf{r}) = \epsilon(\mathbf{r}_\perp)$, and it is the square of the transverse refractive index profile, $\epsilon(\mathbf{r}_\perp) = n^2(\mathbf{r}_\perp)$.

In a paraxial regime, the slowly varying amplitude $\psi(\mathbf{r})$ satisfies the following equation

$$\nabla_{\perp}^2 \psi + 2ik_0 n_0 \nabla_z \psi + (n^2(\mathbf{r}_{\perp}) - n_0^2) k_0 \psi = 0. \quad (1.24)$$

Therefore, we can make a Schrödinger-like wave equation⁹

$$i \frac{\partial \psi}{\partial z} = \left[-\frac{1}{2k_0 n_0} \nabla_{\perp}^2 - \frac{n^2(\mathbf{r}_{\perp}) - n_0^2}{n_0} k_0 \right] \psi = H \psi. \quad (1.25)$$

This shows the refractive index in photonics acts as a potential in quantum mechanics, and non-Hermitian optical system requires complex refractive indices. Therefore, PT -symmetry of the system is achieved by balanced optical gain and loss.

Let us consider the simplest case of two-coupled system with balanced gain and loss. The Hamiltonian for the coupled system can be formulated by 2×2 matrix:¹⁰

$$H = \begin{pmatrix} \delta + i\gamma & \kappa \\ \kappa^* & \delta - i\gamma \end{pmatrix}, \quad (1.26)$$

where δ is a detuning parameter, γ is a gain or loss coefficient, and κ is a coupling strength. The eigenvalues of the Hamiltonian are $\lambda_{\pm} = \delta \pm \sqrt{|\kappa|^2 - \gamma^2}$, and the system possesses two phases: PT -symmetric ($|\kappa| > \gamma$) and PT -broken phase ($|\kappa| < \gamma$). If gain and loss contrast is small compared to the coupling strength, two real eigenvalues appear and the corresponding eigenstates respect PT -symmetry. However, when the gain and loss contrast grow bigger, two complex conjugate eigenvalues appear and they lose PT -symmetry. The transition point at $|\kappa| = \gamma$ is called an exceptional point, where two eigenstates coalesce to become degenerate.

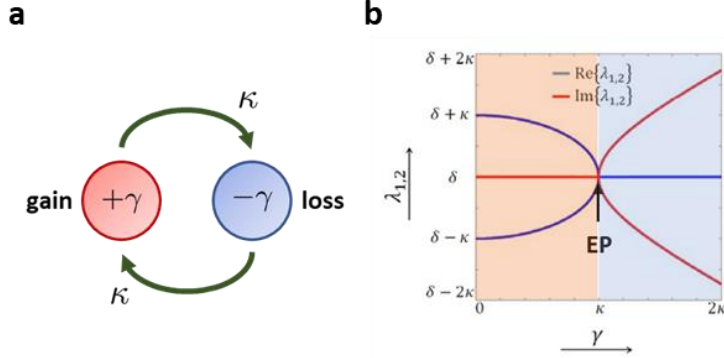


Figure 2 (a) Two coupled system composed of gain and loss. (b) Real and imaginary part of the eigenmodes as a function of the gain and loss coefficient.

The implementation of non-Hermitian system in photonics has brought out numerous applications such as asymmetric mode switching,¹¹ negative refraction,¹² orbital angular momentum micro-laser,¹³ and optical spin black hole.¹⁴ Doppler and his coworkers demonstrated asymmetric mode switching depending on the propagation direction with a systematically deformed waveguide. They utilized the chirality of adiabatic transition, which refers to differential responses with respect to the encircling direction and the initial condition. Since an infinitesimally small nonadiabatic coupling can be exponentially amplified in the gain medium, it causes the gain eigenvector to dominate and the breakdown of adiabaticity. The slow variation of boundary parameters along the propagation direction makes the wave encircle the exceptional point, and right propagation results in counter-clockwise encircling while left propagation results in clockwise encircling. As a result, the output mode is determined by the propagation direction in the waveguide.¹¹ Negative refraction, typically demonstrated by the bulk double-negative metamaterials, is also realized by the PT -symmetric non-Hermitian medium,¹² and the ring with alternative PT -symmetric media generates optical vortex via the unidirectional power oscillation at the exceptional point.¹³ Intriguingly, we can create optical-

spin black hole, where arbitrary polarization states converge into left-handed circular polarization, with strong LCP chirality near the exceptional point.¹⁴

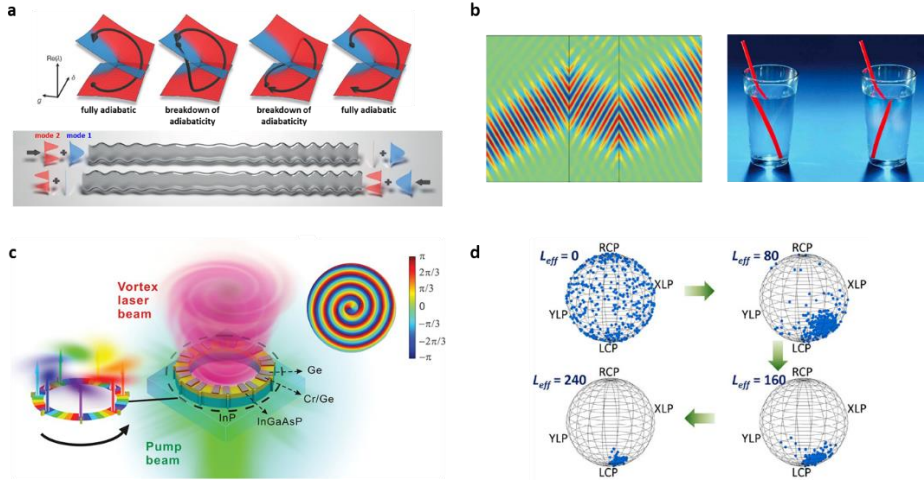


Figure 3 Previous research of non-Hermitian photonics. (a) Asymmetric mode switching. (b) Negative refraction. (c) Orbital angular momentum micro-laser. (d) Optical-spin black hole.

1.3 Non-Hermitian Approach for Plasmonics

Recently, the PT -symmetric non-Hermitian concept is attracting increasing interest in the field of plasmonics due to its potential for novel applications such as ultra-sensitive molecular sensing. In principle, a PT -symmetric Hamiltonian requires balanced gain and loss. Practically, the realization of an ideal gain and loss balanced system is nearly impossible due to inescapable manufacturing imperfections. It is only recently that people found that the PT -symmetric features can also be realized in the imbalanced gain and loss by subtracting gain or loss offset.¹⁵ For example, the Hamiltonian of the two coupled pumped system can be represented by

$$\begin{aligned}
 H_T &= \begin{pmatrix} \delta + i\gamma_1 & \kappa \\ \kappa^* & \delta + i\gamma_2 \end{pmatrix} = H_G + H_{PT} \\
 &= \begin{pmatrix} +i\frac{\gamma_+}{2} & 0 \\ 0 & +i\frac{\gamma_+}{2} \end{pmatrix} + \begin{pmatrix} \delta + i\frac{\gamma_-}{2} & \kappa \\ \kappa^* & \delta - i\frac{\gamma_-}{2} \end{pmatrix}, \tag{1.27}
 \end{aligned}$$

where $\gamma_+ = \gamma_1 + \gamma_2$ is the sum of gains, and $\gamma_- = \gamma_1 - \gamma_2$ is the gain contrast. The total Hamiltonian H_T is divided into a gain offset H_G and a PT -symmetric Hamiltonian H_{PT} . This is called an “active” PT -symmetric system. Likewise, a passive PT -symmetric system is composed of coupled imbalanced lossy system. In the case of two coupled dissipative system, a PT -symmetric Hamiltonian is achieved by subtracting the loss offset H_L :

$$\begin{aligned}
H_T &= \begin{pmatrix} \delta - i\gamma_1 & \kappa \\ \kappa^* & \delta - i\gamma_2 \end{pmatrix} = H_L + H_{PT} \\
&= \begin{pmatrix} -i\frac{\gamma_+}{2} & 0 \\ 0 & -i\frac{\gamma_+}{2} \end{pmatrix} + \begin{pmatrix} \delta + i\frac{\gamma_-}{2} & \kappa \\ \kappa^* & \delta - i\frac{\gamma_-}{2} \end{pmatrix}. \tag{1.28}
\end{aligned}$$

This shows that plasmonic materials which has appreciable dissipation losses can be forged into passive PT -symmetric systems.

In their seminal paper of 2020, Park and coworkers investigated the exceptional point of plasmonic coupled rods array.¹⁶ They utilized two nano-rods in optically different environment, and observed an exceptional point by controlling the displacement between the coupled nano-rods and the periodicity of the array. The coupled system creates hybridized plasmon modes composed of bonding and anti-bonding mode. The upper rod is displaced from the lower one along the lateral direction, and it interacts not only with its counterpart but with other lower one of the neighboring unit. As a consequence, the anti-bonding mode feels attraction with its neighbor while the bonding mode feels repulsion. This causes the interference of the bonding and anti-bonding mode since the attraction lowers the energy of the anti-bonding mode whereas the repulsion increases the energy of the bonding mode.

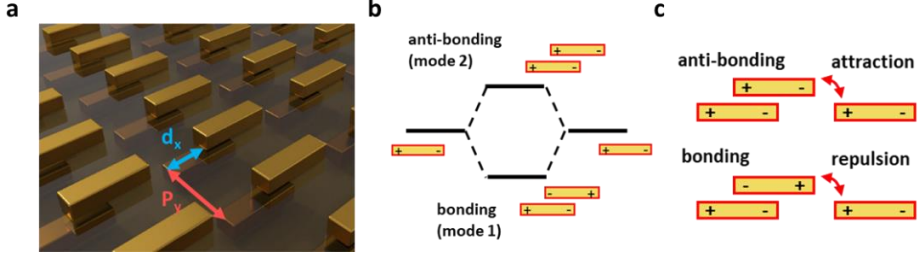


Figure 4 (a) Schematic of coupled nanorods array. (b) Hybridization of the coupled plasmon modes. (c) Mode interference between bonding and anti-bonding mode.

The system can be described by the following 2×2 matrix of Hamiltonian:

$$H = \begin{pmatrix} \delta - i\gamma_1 & \kappa \\ \kappa^* & \delta - i\gamma_2 \end{pmatrix}, \quad (1.29)$$

where δ is the detuning of each plasmon rod, κ is the coupling strength of the coupled rods, and γ_1, γ_2 stand for the loss coefficient of the upper and lower rod, respectively. The modulation of the coupling strength and the loss coefficients dictates the eigenstates and makes the exceptional point. The displacement d_x is related to the coupling strength κ , and as d_x increases, κ decreases because the coupling strength gets weaker. The in-plane periodicity P_y is related to the loss coefficient γ_1 , and as P_y increases, γ_1 decreases because it reduces the number density of lower rods. The real and imaginary parts of the eigenmodes of the plasmonic array refer to the resonance frequency and the loss rate, and Fig. 5 represents them as a function of d_x and P_y . The hybridization of the coupled resonators allows two hybrid modes to be intertwined with each other and generate an exceptional point where both the resonance frequency and loss rate become degenerate.

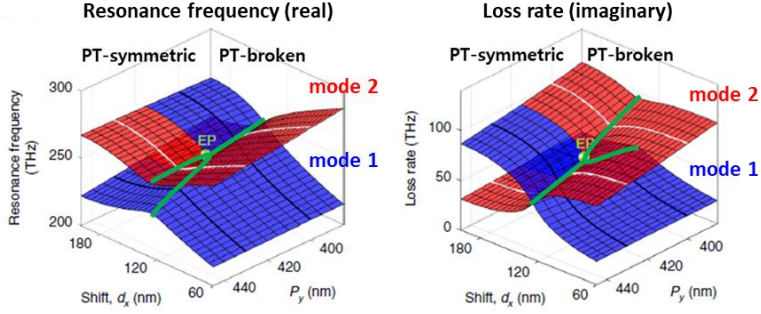


Figure 5 The resonance frequency (left) and loss rate (right) as a function of lateral shift d_x and the y-direction periodicity P_y

The existence of a plasmonic exceptional point is demonstrated by analyzing the behavior of resonance frequency and the loss rate as a function of d_x and P_y . For $P_y = 400$ nm, a crossing of the resonance frequency and an anti-crossing of the loss rate are observed, which is represented by blue lines in Fig. 6 (a). On the other hand, an anti-crossing of the resonance frequency and a crossing of the loss rate are observed for $P_y = 430$ nm, which is represented by green lines in Fig. 6 (a). This confirms that the exceptional point exists between 400 nm and 430 nm for P_y .

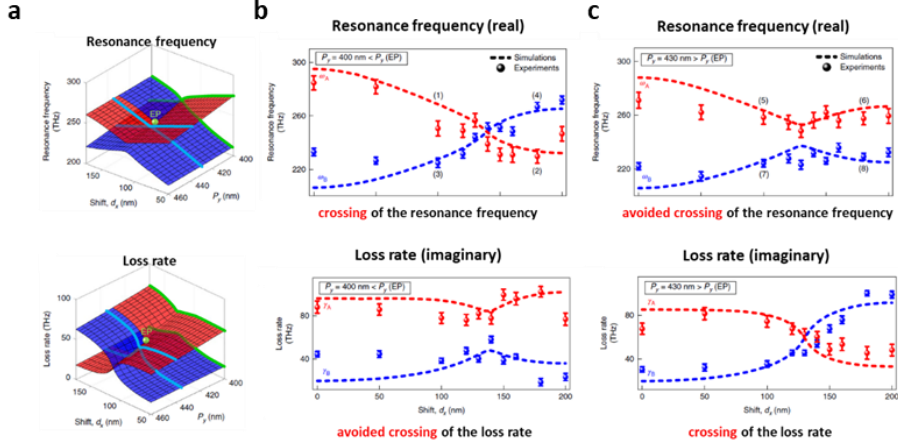


Figure 6 (a) EP Diagram of the resonance frequencies and loss rates. Real and imaginary part of the plasmon modes as a function of d_x (b) for $P_y = 400$ nm, (c) for $P_y = 430$ nm.

This plasmonic exceptional point allows us to demonstrate cutting-edge optical applications, in particular, ultra-sensitive biomolecular sensors. According to the perturbation theory, a perturbed Hamiltonian can be expressed by a Taylor-series expansion. In a typical Hermitian system, the resonance mode is represented by a Taylor-series with respect to the perturbation ϵ ,

$$\omega_n = \omega_{n0} + \epsilon \omega_{n1} + \epsilon^2 \omega_{n2} + \dots, \quad (1.30)$$

and the second and higher order terms are neglected by assuming that the perturbation is sufficiently small. This results in the mode shift linearly proportional to the perturbation. However, in a non-Hermitian system which possesses an N^{th} order exceptional point, a Hamiltonian of the resonance mode can be expressed as:

$$\omega_n = \omega_{n0} + \epsilon^{1/N} \omega_{n1} + \epsilon^{2/N} \omega_{n2} + \dots. \quad (1.31)$$

If we neglect higher order terms in the same manner, one can see that the mode shift is proportional to the N^{th} root of the perturbation.

Stemmed from the properties of the exceptional point, the study evaluated the sensitivity of the plasmonic EP nano-sensor compared to the conventional DP sensor. They were functionalized with anti-immunoglobulin G (IgG) and tested with various concentrations. At large concentration, larger energy splitting for the DP sensor is observed. Then, as the concentration is decreased, larger splitting for the EP sensor is observed below a certain point. This result is consistent with the perturbation theory regarding the exceptional point mentioned above. It shows the EP sensor is more sensitive than the conventional sensors at lower concentrations, and it is believed to lower the detection limit and enable the exploration at small scales.

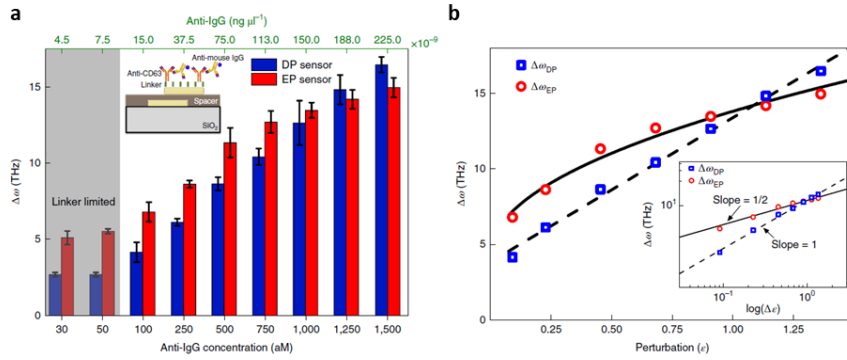


Figure 7 (a) Comparison of mode shift between DP and EP sensor. (b) Mode shift as a function of perturbation for DP and EP sensor.

1.4 Bibliography

- (1) Bender, C. M. *PT Symmetry: In Quantum and Classical Physics*; World Scientific, 2019.
- (2) Bender, C. M.; Boettcher, S. Real Spectra in Non-Hermitian Hamiltonians Having P T Symmetry. *Phys. Rev. Lett.* **1998**, *80* (24), 5243.
- (3) Bender, C. M.; Brod, J.; Bender, C. M.; Dorey, P.; Dunning, C.; Xu, H. S.; Jin, L. Reports on Progress in Physics Related Content Making Sense of Non-Hermitian Hamiltonians Making Sense of Non-Hermitian Hamiltonians. **2007**. <https://doi.org/10.1088/0034-4885/70/6/R03>.
- (4) Bender, C. M.; Brody, D. C.; Jones, H. F. Complex Extension of Quantum Mechanics. *Phys. Rev. Lett.* **2002**, *89* (27), 270401.
- (5) Klaiman, S.; Günther, U.; Moiseyev, N. Visualization of Branch Points in PT-Symmetric Waveguides. *Phys. Rev. Lett.* **2008**, *101* (8), 1–4. <https://doi.org/10.1103/PhysRevLett.101.080402>.
- (6) Guo, A.; Salamo, G. J.; Duchesne, D.; Morandotti, R.; Volatier-Ravat, M.; Aimez, V.; Siviloglou, G. A.; Christodoulides, D. N. Observation of PT-Symmetry Breaking in Complex Optical Potentials. *Phys. Rev. Lett.* **2009**, *103* (9), 1–4. <https://doi.org/10.1103/PhysRevLett.103.093902>.
- (7) Rüter, C. E.; Makris, K. G.; El-Ganainy, R.; Christodoulides, D. N.; Segev, M.; Kip, D. Observation of Parity-Time Symmetry in Optics. *Nat. Phys.* **2010**, *6* (3), 192–195. <https://doi.org/10.1038/nphys1515>.
- (8) Marte, M. A. M.; Stenholm, S. Paraxial Light and Atom Optics: The Optical Schrödinger Equation and Beyond. *Phys. Rev. A - At. Mol. Opt.*

- Phys.* **1997**, *56* (4), 2940–2953.
<https://doi.org/10.1103/PhysRevA.56.2940>.
- (9) Feng, L.; El-Ganainy, R.; Ge, L. Non-Hermitian Photonics Based on Parity-Time Symmetry. *Nat. Photonics* **2017**, *11* (12), 752–762.
<https://doi.org/10.1038/s41566-017-0031-1>.
 - (10) El-Ganainy, R.; Makris, K. G.; Khajavikhan, M.; Musslimani, Z. H.; Rotter, S.; Christodoulides, D. N. Non-Hermitian Physics and PT Symmetry. *Nat. Phys.* **2018**, *14* (1), 11–19.
<https://doi.org/10.1038/NPHYS4323>.
 - (11) Doppler, J.; Mailybaev, A. A.; Böhm, J.; Kuhl, U.; Girschik, A.; Libisch, F.; Milburn, T. J.; Rabl, P.; Moiseyev, N.; Rotter, S. Dynamically Encircling an Exceptional Point for Asymmetric Mode Switching. *Nature* **2016**, *537* (7618), 76–79. <https://doi.org/10.1038/nature18605>.
 - (12) Fleury, R.; Sounas, D. L.; Alù, A. Negative Refraction and Planar Focusing Based on Parity-Time Symmetric Metasurfaces. *Phys. Rev. Lett.* **2014**, *113* (2), 1–5. <https://doi.org/10.1103/PhysRevLett.113.023903>.
 - (13) Miao, P.; Zhang, Z.; Sun, J.; Walasik, W.; Longhi, S.; Litchinitser, N. M.; Feng, L. Orbital Angular Momentum Microlaser. *2017 Conf. Lasers Electro-Optics, CLEO 2017 - Proc.* **2017**, *2017-January* (6298), 1–2.
https://doi.org/10.1364/CLEO_SI.2017.SW1C.3.
 - (14) Yu, S.; Park, H. S.; Piao, X.; Min, B.; Park, N. Low-Dimensional Optical Chirality in Complex Potentials. *Optica* **2016**, *3* (9), 1025.
<https://doi.org/10.1364/optica.3.001025>.
 - (15) Ornigotti, M.; Szameit, A. Quasi PT-Symmetry in Passive Photonic

Lattices. *J. Opt. (United Kingdom)* **2014**, *16* (6).

<https://doi.org/10.1088/2040-8978/16/6/065501>.

- (16) Park, J. H.; Ndao, A.; Cai, W.; Hsu, L.; Kodigala, A.; Lepetit, T.; Lo, Y. H.; Kanté, B. Symmetry-Breaking-Induced Plasmonic Exceptional Points and Nanoscale Sensing. *Nat. Phys.* **2020**, *16* (4), 462–468.
<https://doi.org/10.1038/s41567-020-0796-x>.
- (17) Luo, Y.; Chi, C.; Jiang, M.; Li, R.; Zu, S.; Li, Y.; Fang, Z. Plasmonic Chiral Nanostructures: Chiroptical Effects and Applications. *Adv. Opt. Mater.* **2017**, *5* (16), 1700040. <https://doi.org/10.1002/adom.201700040>.

Chapter 2. Chiral Plasmonics

2.1 Chirality and Chiral Plasmonics

Chirality is the symmetry property of an object, which has its non-superimposable mirror image.¹ Mathematically, a chiral object is not overlapped by simple rotations or translations alone. Apart from the geometrical point of view, chirality also manifests itself in chemical properties. The chirality has started to get noticed since it played a crucial role in chemical and pharmaceutical industries. Thalidomide tragedy is a case in point.² Thalidomide was firstly intended to treat morning sickness in pregnant women, but it caused serious side effects represented by birth defects. While the *R*-Thalidomide served the intended efficacy, the enantiomer *S*-Thalidomide caused the birth of deformed children. This suggests that synthesizing and separating pure chiral enantiomer is a crucial in chemical and pharmaceutical industry.

Also, the chirality manifests itself while interacting with traveling light. The chiral molecules exhibit a different response to left or right circularly polarized (LCP and RCP) light, and different complex refractive indices were obtained for those polarization states.³ The difference in the real part results in the rotation of the linearly polarized light traveling through the medium, which is called optical rotatory dispersion (ORD). Also, circular dichroism (CD), which refers to the different absorption of LCP and RCP light, appears from the difference of the imaginary parts. CD and ORD spectroscopy are widely utilized for not only detecting chiral molecules but also studying the structures and conformation of macromolecules such as peptides or proteins.⁴ However, the chiroptical signals of those molecules are very weak, so a large amount of analyte is required for the studying.

In this context, plasmonic nanostructures have been utilized to solve many of these problems. Plasmonic materials such as gold, silver and platinum have their own intriguing optical properties originated from the plasmonic resonance.⁵ This resonance concentrates the electromagnetic radiation into the subwavelength scales, and induces strong electric field enhancement. Also, the resonances of individual particles can form collective modes by the near-field coupling and exhibit strong optical responses extending over the entire nanostructure. Therefore, Plasmonic nanomaterials can be utilized to enhance the weak chiroptical signals of chiral molecules.

Chiral plasmonics has been emerged as an extension of these efforts. The integration of a chiral structure with a plasmonic material is required for this purpose, since plasmonic material exhibits intense structure-related optical responses stemmed from strong light-matter interaction. The chiral plasmonic nanostructures strongly distort electromagnetic nearfield and form a twisted field, which is called “superchiral field”.⁶ This superchiral field provides distinctly different optical environment for chiral molecules, and recent researches have utilized this concept to distinguish chiral molecules in the superchiral field region. Hendry and coworkers manufactured gold gammadion nanostructures and studied the secondary structures of proteins.⁷ This chiral spectroscopy methodology has been utilized to analyze the fingerprint of the three-dimensional structures of biomolecules (Figure 8).

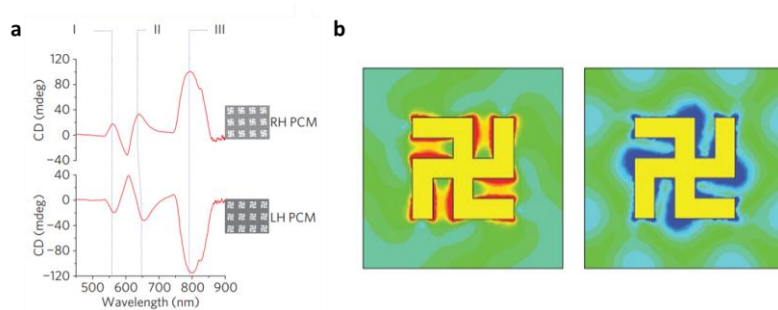


Figure 8 Chiroptical responses of the constructed gold gammadion nanostructures, (a) CD spectra for left- and right-handed PCM. (b) Electric field and optical chirality distribution at III.

2.2 Fabrication of Chiral Nanostructures

The aforementioned chiral plasmonic nanostructure can be produced by various techniques, and many of them have been fabricated by top-down method such as e-beam lithography and direct laser writing.⁸⁻¹⁰ By virtue of the significant development of nano-fabrication techniques, top-down fabrication approach manufactures well-organized and complicated chiral nanostructures. Hentschel and coworkers generated chiral plasmonic oligomers using electron beam lithography.⁸ The chiral nanostructure was assembled by layer-by-layer stacking. On the first layer, 3 nano-discs were arranged to form an L-shape, and on the second layer, the fourth nano-disc was located on top of one of the nano-discs which dictates the handedness of the nanostructure. Also, Gansel and coworkers fabricated three-dimensional helical structures using direct laser writing and electroplating.⁹ The constructed structures exhibit free-standing helical nano-morphology which are uniformly rotated around the vertical axis.

Although a variety of chiral nanostructures have been constructed by Top-down approach, Bottom-up approach has emerged to resolve the issue of limited resolution and high fabrication cost.¹¹⁻¹³ The assembly of nanoparticles exhibits apparent chirality with respect to the orientation, and the chiroptical properties are directly related to the geometrical orientations of the constituent nanoparticles. Therefore, the chiral self-assembly of nanoparticles can produce sophisticated chiral structures at the sub-wavelength scale. Wang and coworkers constructed chiral templates composed of nanofibril structures using a peptide sequence.¹¹ When gold nanoparticles and the nanofibril structures were mixed together, the Au nanoparticles were arranged into a double helical structure along the template. Liedl and coworkers constructed DNA origami structures with plasmonic nanoparticles, and they exhibited strong CD signals originated from a three-dimensional helical arrangement.¹³

Despite of numerous trials for chiral nanostructure fabrication, large-scale and simple fabrication methods for three-dimensional chiral structures have been hard to be achieved. In this regard, Chirality transfer was proposed as a simpler and more effective alternative.¹⁴ Lee and coworkers synthesized chiral gold nanoparticles using chiral amino acids and peptides.¹⁵ The chiral molecules were attached to the surface of gold nanoparticles and induced asymmetric evolution of nanoparticles to form chiral morphologies. The synthesized nanoparticles featured strong chiroptical responses stemmed from the twisted chiral gaps. They exhibited giant dissymmetry factor of 0.2, even when dispersed in random orientation, and strong circular dichroic peak was observed at visible wavelength. This synthesis method is especially notable that the chiral structures can be elaborately controlled at nanometer scale.

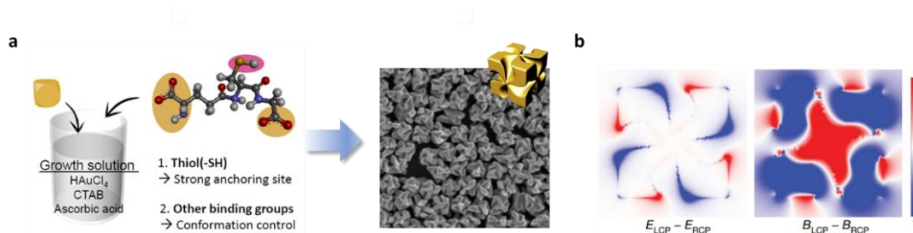


Figure 9 (a) Synthesis of chiral gold nanoparticles. (b) Calculated chiroptical distribution of the chiral nanoparticles¹⁷

To understand the chiroptical properties of the synthesized nanoparticles, we conducted optical simulations using finite element method-based three-dimensional Maxwell equation solver (COMSOL). The multipole analysis of the scattering of chiral nanoparticles under planewave incidence indicates that the chiroptical properties are derived from the interference of electric dipole and magnetic dipole moments. In terms of parity symmetry, the multipole moments can be categorized into odd and even parity, and electric dipole has odd parity while magnetic dipole has even parity. The interference of

odd and even parity multipole moments produce chiroptical responses.¹⁶ At 560 nm, where the electric dipole moment is dominant, the polarization current density vectors are parallelly aligned to the electric field. On the other hand, at 590 nm, the polarization current density vectors form current loops around the chiral gaps which leads to the formation of magnetic dipoles. However, due to the sophisticated structures of the chiral nanoparticles, it has been challenging for studying the mechanism of the chiroptical responses and utilizing them in the field of chiral plasmonics. This leaves the need for simplified models to describe the chiroptical phenomena.

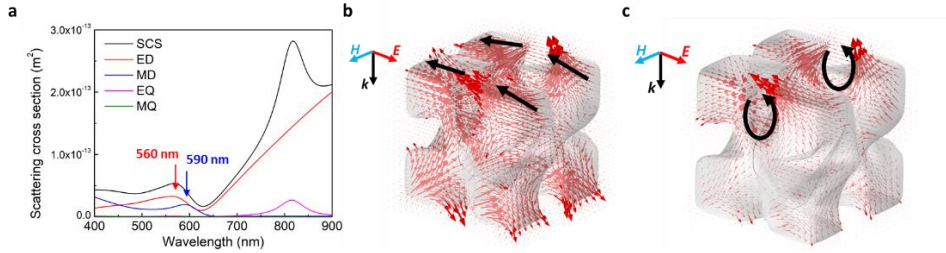


Figure 10 (a) Multipole analysis of the scattering cross-section of 432 helicoid III. Polarization current distribution (b) at 560 nm, (c) at 590 nm.

2.3 The Simplest Chiral Model: Born-Kuhn Model

In this section, we are going to discuss the simplest theoretical model which describes the chiral objects. About a century ago, in order to describe chiral molecules, Born devised a coupled oscillator model based on the perturbation theory,¹⁷ and Kuhn reorganized the model and simplified it into two orthogonally oscillating coupled oscillators.¹⁸ Recently, Yin and coworkers applied the model into the plasmonic nanorods and suggested that it can be utilized for analytic studying.¹⁹

This model is derived from the Drude-Lorentz model, which deals with a damped harmonic oscillation of an electron. Under an external electric field \mathbf{E}_0^{ext} , the motion of an electron \mathbf{u} satisfies the following relation:

$$\partial_t^2 \mathbf{u} + \gamma \partial_t \mathbf{u} + \omega_0^2 \mathbf{u} = -\frac{e}{m^*} \mathbf{E}_0^{ext} e^{-i\omega t}, \quad (2.1)$$

where γ is a damping coefficient, ω_0 is the natural frequency, e is the charge of an electron, and m^* is the effective mass. This is widely used for analyzing the optical properties of metal nanoparticles. Born-Kuhn model couples two orthogonally aligned Drude-Lorentz oscillator. A resonator oscillates in x-direction while the other oscillates in y-direction and they are separated by a distance d in z-direction, which is the longitudinal direction of the incident electromagnetic wave:

$$\begin{aligned} \partial_t^2 u_x + \gamma \partial_t u_x + \omega_0^2 u_x + \omega_c^2 u_y &= -\frac{e}{m^*} E_{0,x}^{ext} e^{i(k(z_0 + \frac{d}{2}) - \omega t)}, \\ \partial_t^2 u_y + \gamma \partial_t u_y + \omega_0^2 u_y + \omega_c^2 u_x &= -\frac{e}{m^*} E_{0,y}^{ext} e^{i(k(z_0 + \frac{d}{2}) - \omega t)}. \end{aligned} \quad (2.2)$$

They are bound with the coupling strength ω_c , and the longitudinal displacement generates the chiroptic responses stemmed from the distinct phase delay for x- and y-direction. The Born-Kuhn model possesses two normal modes, which are bonding and anti-bonding mode, and each mode selectively responds to left- or right-handed circularly polarized light.

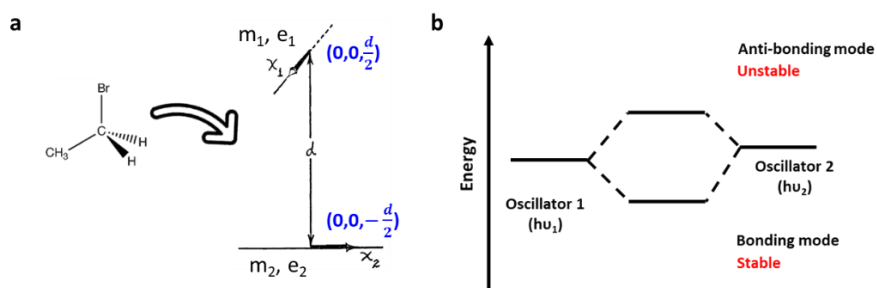


Figure 11 (a) Devised Born-Kuhn model for the description of chiral molecules.
(b) Mode hybridization of Born-Kuhn model.

2.4 Extended Born-Kuhn Models

Although the Born-Kuhn model had successfully reproduced the chiroptical properties of the solution of chiral molecules, the pitfalls of the model have been clearly recognized when the behavior of the individual particles is considered. The configuration of chiral particles with respect to the incident light is strictly related to the optical responses, but the Born-Kuhn model cannot embrace the entire circumstances since the oscillators only covers two axes, i.e. x- and y-axis, in three-dimensional space. For instance, the Born-Kuhn model displays vanished circular dichroic values when the light is incident at right angle.

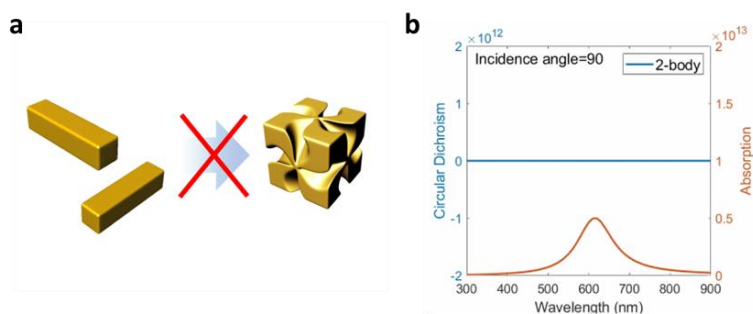


Figure 12 (a) Born-Kuhn model does not fully describe 3-dimensional chiral materials. (b) Optical properties of Born-Kuhn model are strongly dependent on the incidence direction.

The problem can be resolved when we implement another oscillator in the model. Moreover, the oscillating directions are not restricted to x, y, or z direction to consider the anisotropic optical properties of the particles. For this model, we coined a term “extended Born-Kuhn model”. In this model, the motions of three oscillators positioned at r_1 , r_2 and r_3 can be formulated by three linear equations:²⁰

$$\begin{aligned}
\partial_t^2 \mathbf{u}_1 + \gamma \partial_t \mathbf{u}_1 + \omega_0^2 \mathbf{u}_1 - \omega_c^2 \mathbf{u}_2 - \omega_c^2 \mathbf{u}_3 &= -\frac{e}{m_*} (\mathbf{E}_0 \cdot \mathbf{a}_1) e^{i(\mathbf{k} \cdot \mathbf{r}_1 - \omega t)}, \\
\partial_t^2 \mathbf{u}_2 + \gamma \partial_t \mathbf{u}_2 + \omega_0^2 \mathbf{u}_2 - \omega_c^2 \mathbf{u}_3 - \omega_c^2 \mathbf{u}_1 &= -\frac{e}{m_*} (\mathbf{E}_0 \cdot \mathbf{a}_2) e^{i(\mathbf{k} \cdot \mathbf{r}_2 - \omega t)}, \\
\partial_t^2 \mathbf{u}_3 + \gamma \partial_t \mathbf{u}_3 + \omega_0^2 \mathbf{u}_3 - \omega_c^2 \mathbf{u}_1 - \omega_c^2 \mathbf{u}_2 &= -\frac{e}{m_*} (\mathbf{E}_0 \cdot \mathbf{a}_3) e^{i(\mathbf{k} \cdot \mathbf{r}_3 - \omega t)},
\end{aligned} \tag{2.3}$$

where the oscillating vector \mathbf{u}_1 , \mathbf{u}_2 , \mathbf{u}_3 and their unit vector \mathbf{a}_1 , \mathbf{a}_2 , \mathbf{a}_3 can point to arbitrary direction, and the wave vector \mathbf{k} is parallel to the incidence direction.

For convenience, a constant is implemented

$$\Omega^2 = \partial_t^2 + \gamma \partial_t + \omega_0^2 = \omega_0^2 - i\gamma\omega - \omega^2. \tag{2.4}$$

Then, the equation can be simply expressed as a matrix equation:

$$\begin{pmatrix} \Omega^2 & -\omega_c^2 & -\omega_c^2 \\ -\omega_c^2 & \Omega^2 & -\omega_c^2 \\ -\omega_c^2 & -\omega_c^2 & \Omega^2 \end{pmatrix} \begin{pmatrix} \mathbf{u}_1 \\ \mathbf{u}_2 \\ \mathbf{u}_3 \end{pmatrix} = -\frac{e}{m_*} \begin{pmatrix} (\mathbf{E}_0 \cdot \mathbf{a}_1) e^{i(\mathbf{k} \cdot \mathbf{r}_1)} \\ (\mathbf{E}_0 \cdot \mathbf{a}_2) e^{i(\mathbf{k} \cdot \mathbf{r}_2)} \\ (\mathbf{E}_0 \cdot \mathbf{a}_3) e^{i(\mathbf{k} \cdot \mathbf{r}_3)} \end{pmatrix} e^{-i\omega t}. \tag{2.5}$$

If we derive the determinant,

$$D = \begin{vmatrix} \Omega^2 & -\omega_c^2 & -\omega_c^2 \\ -\omega_c^2 & \Omega^2 & -\omega_c^2 \\ -\omega_c^2 & -\omega_c^2 & \Omega^2 \end{vmatrix} = \Omega^2 - 3\omega_c^4 \Omega^2 - 2\omega_c^6. \tag{2.6}$$

The solutions of the extended Born-Kuhn model are found to be

$$\begin{aligned}
\mathbf{u}_1 &= -\frac{e}{m^* D} [(\Omega^4 - \omega_c^4)(\mathbf{E}_0 \cdot \mathbf{a}_1)e^{i(\mathbf{k} \cdot \mathbf{r}_1)} + (\omega_c^4 + \omega_c^2 \Omega^2)(\mathbf{E}_0 \cdot \mathbf{a}_2)e^{i(\mathbf{k} \cdot \mathbf{r}_2)} \\
&\quad + (\omega_c^4 + \omega_c^2 \Omega^2)(\mathbf{E}_0 \cdot \mathbf{a}_3)e^{i(\mathbf{k} \cdot \mathbf{r}_3)}] e^{-i\omega t} \mathbf{a}_1, \\
\mathbf{u}_2 &= -\frac{e}{m^* D} [(\Omega^4 - \omega_c^4)(\mathbf{E}_0 \cdot \mathbf{a}_2)e^{i(\mathbf{k} \cdot \mathbf{r}_2)} + (\omega_c^4 + \omega_c^2 \Omega^2)(\mathbf{E}_0 \cdot \mathbf{a}_3)e^{i(\mathbf{k} \cdot \mathbf{r}_3)} \\
&\quad + (\omega_c^4 + \omega_c^2 \Omega^2)(\mathbf{E}_0 \cdot \mathbf{a}_1)e^{i(\mathbf{k} \cdot \mathbf{r}_1)}] e^{-i\omega t} \mathbf{a}_2, \\
\mathbf{u}_3 &= -\frac{e}{m^* D} [(\Omega^4 - \omega_c^4)(\mathbf{E}_0 \cdot \mathbf{a}_3)e^{i(\mathbf{k} \cdot \mathbf{r}_3)} + (\omega_c^4 + \omega_c^2 \Omega^2)(\mathbf{E}_0 \cdot \mathbf{a}_1)e^{i(\mathbf{k} \cdot \mathbf{r}_1)} \\
&\quad + (\omega_c^4 + \omega_c^2 \Omega^2)(\mathbf{E}_0 \cdot \mathbf{a}_2)e^{i(\mathbf{k} \cdot \mathbf{r}_2)}] e^{-i\omega t} \mathbf{a}_3.
\end{aligned} \tag{2.7}$$

This coupled motion of electrons generates oscillating current density:

$$\mathbf{J} = -ne \left[\frac{\partial \mathbf{u}_1}{\partial t} \Big|_{\mathbf{r}_0 = \mathbf{r} - \delta \mathbf{r}_1} + \frac{\partial \mathbf{u}_2}{\partial t} \Big|_{\mathbf{r}_0 = \mathbf{r} - \delta \mathbf{r}_2} + \frac{\partial \mathbf{u}_3}{\partial t} \Big|_{\mathbf{r}_0 = \mathbf{r} - \delta \mathbf{r}_3} \right], \tag{2.8}$$

and the extinction power is obtained in terms of the current density and the incident field $\mathbf{E}_{inc} = \mathbf{E}_0 e^{-i\omega t}$ from the reciprocity theorem,²¹

$$P = \frac{1}{2} \Re \left\{ \iiint_V \mathbf{J}^* \cdot \mathbf{E}_{inc} dV \right\} = \frac{1}{2} \Re \left\{ (\mathbf{J}^* \cdot \mathbf{E}_{inc}) V \right\}, \tag{2.9}$$

where we assume the uniform current density in the entire volume V of the coupled system. The incident circularly polarized light is expressed as Jones vector:

$$\mathbf{E}_{LCP} = \begin{pmatrix} E_x \\ E_y \\ E_z \end{pmatrix} = \frac{1}{\sqrt{2}} E_0 \begin{pmatrix} 1 \\ -i \\ 0 \end{pmatrix}, \quad \mathbf{E}_{RCP} = \begin{pmatrix} E_x \\ E_y \\ E_z \end{pmatrix} = \frac{1}{\sqrt{2}} E_0 \begin{pmatrix} 1 \\ +i \\ 0 \end{pmatrix} = \mathbf{E}_{LCP}^*. \tag{2.10}$$

Therefore, the circular dichroism is obtained by

$$CD = P_{LCP} - P_{RCP} = \frac{1}{2} \Re \left\{ \mathbf{J}^* \cdot (\mathbf{E}_{LCP} - \mathbf{E}_{RCP}) V \right\}. \quad (2.11)$$

The obtained circular dichroism result indicates that for normal incidence, the extended Born-Kuhn model displays the same responses as the Born-Kuhn model, but for oblique incidence, it shows stronger circular dichroism than the previous Born-Kuhn model. Furthermore, the CD response does not vanish for right angle incidence.

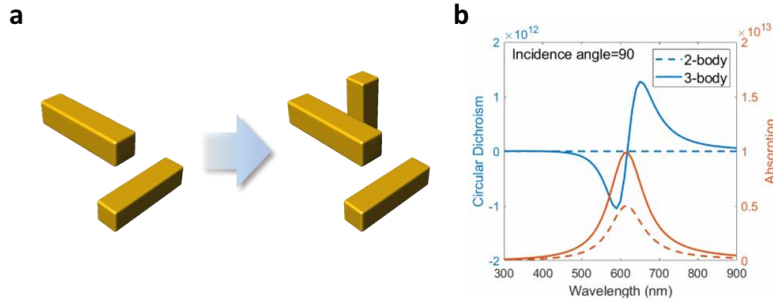


Figure 13 (a) Implementation of the extended Born-Kuhn model. (b) Comparison of optical properties of Born-Kuhn model and the extended Born-Kuhn model.

In particular, we devised “432 Born-Kuhn model” to reproduce the optical properties of chiral nanoparticles. From a geometric point of view, the synthesized chiral nanoparticles possess 432 point group symmetry: 4-fold symmetry along $\langle 100 \rangle$ axes, 3-fold symmetry along $\langle 111 \rangle$ axes and 2-fold symmetry along $\langle 110 \rangle$ axes.²² The 432 Born-Kuhn model was designed to represent the 432 symmetry of the nanoparticles. It was constructed by the successive 3-fold rotation around $[111]$ axis, 4-fold rotation around $[001]$ axis and 2-fold rotation around $[010]$ axis of the symmetry unit.

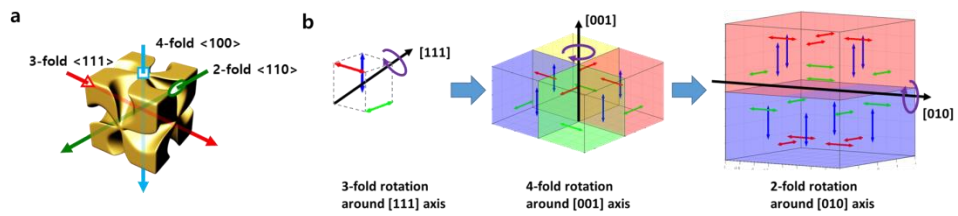


Figure 14 (a) 432 symmetry of 432 helicoid III. (b) Construction of 432 Born-Kuhn model by the successive 3-fold, 4-fold, and 2-fold rotation.

2.5 Objective of Thesis

The primary goal of this thesis is to establish fundamental understanding of the role of chiral plasmonic nanomaterials in non-Hermitian photonics. Although there has been increasing number of researches on the non-Hermitian photonics, the non-Hermitian systems of plasmonic materials are not well understood. Moreover, the implementation of non-Hermitian concept to chiral plasmonics produces far more sophisticated circumstances to be analyzed. This thesis is a preliminary attempt to develop a theoretical framework of chiral non-Hermitian photonics. Therefore, we focused on the analysis of non-Hermitian characteristic of chiral nanostructures, in particular, the behavior of exceptional points with respect to the chirality. First, for the sake of simplicity, the chiral nanostructures were reduced to Born-Kuhn model, which was discussed in Chapter 2.3. Then, we analyzed the Born-Kuhn model via theoretical and numerical methodologies. In theoretical approach, we applied coupled mode theory to investigate the exceptional point of the Born-Kuhn model. Depending on left- and right-handed circularly polarized light, different exceptional points were theoretically derived. In order to support the theoretical prediction, numerical calculation using finite element method-based Maxwell equation solver was conducted. We constructed the array of the Born-Kuhn model and tuned two parameters: the lateral displacement of the first and the second rod and the periodicity in y-direction, and calculated transmission coefficients (or S-parameters) from the optical simulation. The exceptional points were obtained from the resulting transmission coefficients, and distinct exceptional points appeared under the illumination of the different circular polarization state. The results indicate that the exceptional points of chiral nanomaterials can be controlled by the spin state of the incident photons.

2.6 Bibliography

- (1) Kelvin, W. T. B. *The Molecular Tactics of a Crystal*; Clarendon Press, 1894.
- (2) Tokunaga, E.; Yamamoto, T.; Ito, E.; Shibata, N. Understanding the Thalidomide Chirality in Biological Processes by the Self-Disproportionation of Enantiomers. *Sci. Rep.* **2018**, 8 (1), 17131. <https://doi.org/10.1038/s41598-018-35457-6>.
- (3) Rodger, A.; Nordén, B. *Circular Dichroism and Linear Dichroism*; Oxford University Press, 1997; Vol. 1.
- (4) Berova, N.; Nakanishi, K.; Woody, R. W. *Circular Dichroism: Principles and Applications*; John Wiley & Sons, 2000.
- (5) Stockman, M. I. Nanoplasmonics: Past, Present, and Glimpse into Future. *Opt. Express* **2011**, 19 (22), 22029–22106.
- (6) Tang, Y.; Cohen, A. E. Optical Chirality and Its Interaction with Matter. *Phys. Rev. Lett.* **2010**, 104 (16), 163901.
- (7) Hendry, E.; Carpy, T.; Johnston, J.; Popland, M.; Mikhaylovskiy, R. V.; Laphorn, A. J.; Kelly, S. M.; Barron, L. D.; Gadegaard, N.; Kadodwala, M. Ultrasensitive Detection and Characterization of Biomolecules Using Superchiral Fields. *Nat. Nanotechnol.* **2010**, 5 (11), 783–787. <https://doi.org/10.1038/nnano.2010.209>.
- (8) Hentschel, M.; Schäferling, M.; Weiss, T.; Kuball, H. G.; Liu, N.; Giessen, H. Three-Dimensional Chiral Plasmonic Oligomers. *Opt. InfoBase Conf. Pap.* **2012**. <https://doi.org/10.1364/qels.2012.qth4f.1>.

- (9) Gansel, J. K.; Thiel, M.; Rill, M. S.; Decker, M.; Bade, K.; Saile, V.; Von Freymann, G.; Linden, S.; Wegener, M. Gold Helix Photonic Metamaterial as Broadband Circular Polarizer. *Science* (80-.). **2009**, 325 (5947), 1513–1515. <https://doi.org/10.1126/science.1177031>.
- (10) Fischer, J.; Mueller, J. B.; Kaschke, J.; Wolf, T. J. A.; Unterreiner, A.-N.; Wegener, M. Three-Dimensional Multi-Photon Direct Laser Writing with Variable Repetition Rate. *Opt. Express* **2013**, 21 (22), 26244. <https://doi.org/10.1364/oe.21.026244>.
- (11) Fu, X.; Wang, Y.; Huang, L.; Sha, Y.; Gui, L.; Lai, L.; Tang, Y. Assemblies of Metal Nanoparticles and Self-Assembled Peptide Fibrils - Formation of Double Helical and Single-Chain Arrays of Metal Nanoparticles. *Adv. Mater.* **2003**, 15 (11), 902–906. <https://doi.org/10.1002/adma.200304624>.
- (12) Kuzyk, A.; Schreiber, R.; Zhang, H.; Govorov, A. O.; Liedl, T.; Liu, N. Reconfigurable 3D Plasmonic Metamolecules. *Nat. Mater.* **2014**, 13 (9), 862–866. <https://doi.org/10.1038/nmat4031>.
- (13) Kuzyk, A.; Schreiber, R.; Fan, Z.; Pardatscher, G.; Roller, E. M.; Högele, A.; Simmel, F. C.; Govorov, A. O.; Liedl, T. DNA-Based Self-Assembly of Chiral Plasmonic Nanostructures with Tailored Optical Response. *Nature* **2012**, 483 (7389), 311–314. <https://doi.org/10.1038/nature10889>.
- (14) Orme, C. A.; Noy, A.; Wierzbicki, A.; McBride, M. T.; Grantham, M.; Teng, H. H.; Dove, P. M.; Deyoreo, J. J. Formation of Chiral Morphologies through Selective Binding of Amino Acids to Calcite Surface Steps. *Nature* **2001**, 411 (6839), 775–779. <https://doi.org/10.1038/35081034>.

- (15) Lee, H. E.; Ahn, H. Y.; Mun, J.; Lee, Y. Y.; Kim, M.; Cho, N. H.; Chang, K.; Kim, W. S.; Rho, J.; Nam, K. T. Amino-Acid- A Nd Peptide-Directed Synthesis of Chiral Plasmonic Gold Nanoparticles. *Nature* **2018**, *556* (7701), 360–364. <https://doi.org/10.1038/s41586-018-0034-1>.
- (16) Barron, L. D. *Molecular Light Scattering and Optical Activity*; Cambridge University Press, 2009.
- (17) Born, M. Über Die Natürliche Optische Aktivität Der Kristalle. *Zeitschrift für Phys.* **1922**, *8* (1), 390–417.
- (18) Kuhn, W. Quantitative Verhältnisse Und Beziehungen Bei Der Natürlichen Optischen Aktivität. *Zeitschrift für Phys. Chemie* **1929**, *4* (1), 14–36.
- (19) Yin, X.; Schäferling, M.; Metzger, B.; Giessen, H. Interpreting Chiral Nanophotonic Spectra: The Plasmonic Born-Kuhn Model. *Nano Lett.* **2013**, *13* (12), 6238–6243. <https://doi.org/10.1021/nl403705k>.
- (20) Davis, M. S.; Zhu, W.; Lee, J. K.; Lezec, H. J.; Agrawal, A. Microscopic Origin of the Chiroptical Response of Optical Media. *Sci. Adv.* **2019**, *5* (10). <https://doi.org/10.1126/sciadv.aav8262>.
- (21) Jackson, J. D. *Classical Electrodynamics*. American Association of Physics Teachers 1999.
- (22) Im, S. W.; Ahn, H.-Y.; Kim, R. M.; Cho, N. H.; Kim, H.; Lim, Y.-C.; Lee, H.-E.; Nam, K. T. Chiral Surface and Geometry of Metal Nanocrystals. *Adv. Mater.* **2019**. <https://doi.org/10.1002/adma.201905758>.

Chapter 3. Non-Hermitian Approach for Born-Kuhn Model

3.1 Coupled Mode Theory

Before we discuss the theoretical demonstration of the exceptional point, in this section, coupled mode theory is briefly introduced. The coupled mode theory is a phenomenological approach to describe the coupling behavior of an optical resonator excited by a radiation (Figure 15 (a)).¹ This can be widely utilized for modeling the optical properties of plasmonic particles.² The time variation of the mode amplitude $a_1(t)$ of a single resonator is expressed by a first order differential equation,

$$\frac{da_1(t)}{dt} = -i\omega_1 a_1(t) - \frac{1}{\tau_1} a_1(t) + \kappa_1 f_0(t), \quad (3.1)$$

where ω_1 is the resonance frequency, τ_1 is the decay time, and κ_1 is the coupling strength with the incident field f_0 .

Applying Fourier transformation, we obtained the mode amplitude and the external disturbance as a function of frequency:

$$\begin{aligned} a_1(t) &= \int \tilde{a}_1(\omega) e^{-i\omega t} d\omega, \\ f_0(t) &= \int \tilde{f}_0(\omega) e^{-i\omega t} d\omega. \end{aligned} \quad (3.2)$$

By substituting them into (3.1), the mode amplitude can be written as a singular function:

$$\tilde{a}_1(\omega) = \frac{i\kappa_1 \tilde{f}_0(\omega)}{\omega - \tilde{\omega}_1}, \quad (3.3)$$

where complex resonance frequency $\tilde{\omega}_1 = \omega_R + i\omega_I = \omega_1 + i(-\frac{1}{\tau_1})$ is defined. The real part of $\tilde{\omega}_1$ refers to the resonance position while the imaginary part to the width of the spectrum. The extinction cross-section corresponds to the imaginary part of the mode amplitude as shown in Figure 15 (b), and the spectral line shape is Lorentzian.

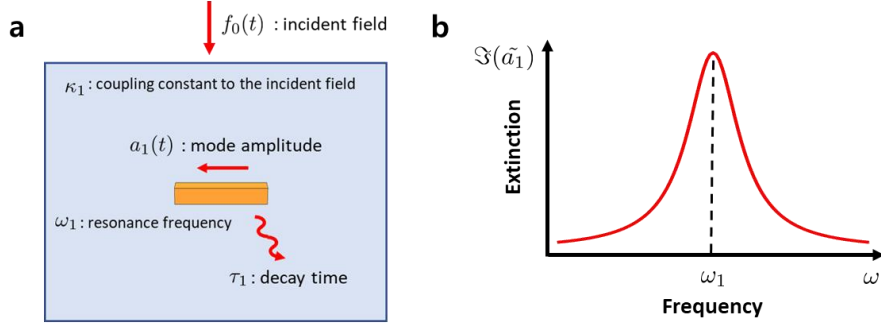


Figure 15 (a) Schematic of the single plasmonic resonator in coupled mode theory and (b) its corresponding extinction spectrum

3.2 Theoretical Demonstration of the Exceptional Point

In this section, we theoretically calculated the exceptional point of the Born-Kuhn model by deriving a set of equations describing the amplitudes of two coupled plasmon modes. We can expand the dynamic equation of a single resonator discussed in Chapter 3.1 as the linear equations of two coupled plasmon modes (Figure 16 (a)),³

$$\begin{aligned}\frac{da_1(t)}{dt} &= -i\omega_1 a_1(t) - \frac{1}{\tau_1} a_1(t) + \kappa_1 f_0(t) + \kappa_{12} a_2(t), \\ \frac{da_2(t)}{dt} &= -i\omega_2 a_2(t) - \frac{1}{\tau_2} a_2(t) + \kappa_2 f_0(t) + \kappa_{21} a_1(t),\end{aligned}\tag{3.4}$$

where the mutual coupling constants κ_{12} and κ_{21} are added. Then, we obtained the Fourier-transformed mode amplitudes and incident fields, and transformed the equations into a matrix equation:

$$\begin{pmatrix} \omega - \tilde{\omega}_1 & -i\kappa_{12} \\ -i\kappa_{21} & \omega - \tilde{\omega}_2 \end{pmatrix} \begin{pmatrix} \tilde{a}_1(\omega) \\ \tilde{a}_2(\omega) \end{pmatrix} = \begin{pmatrix} i\kappa_1 \\ i\kappa_2 \end{pmatrix} \tilde{f}_0(\omega).\tag{3.5}$$

Finally, we solved the matrix equation, and the resulting mode amplitude for each resonator is written as a sum of two singular functions,

$$a_1(\omega) = \frac{\tilde{a}_1^+}{\omega - \tilde{\omega}^+} + \frac{\tilde{a}_1^-}{\omega - \tilde{\omega}^-}, \quad a_2(\omega) = \frac{\tilde{a}_2^+}{\omega - \tilde{\omega}^+} + \frac{\tilde{a}_2^-}{\omega - \tilde{\omega}^-}.\tag{3.6}$$

These solutions indicate that the mutual coupling generates two hybrid modes, typically, bonding and anti-bonding mode, for each resonator. The resonance frequencies of the hybrid modes are distinct from the original modes, and the total extinction cross-section, which corresponds to the sum of the imaginary

parts of the mode amplitudes, $\Im(\tilde{a}_1 + \tilde{a}_2)$, shows two resonance peaks at ω^- and ω^+ (Figure 16 (b)).

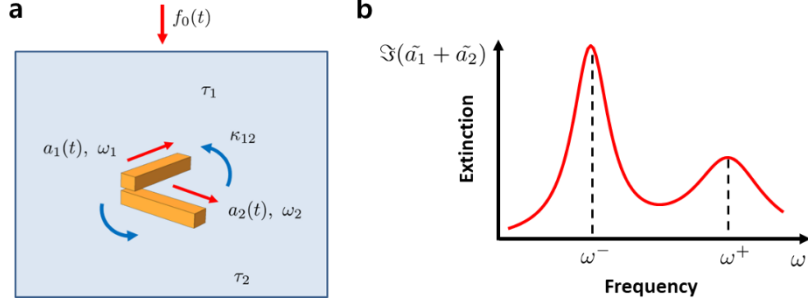


Figure 16 (a) Schematic of Born-Kuhn model described by the coupled mode theory. (b) Extinction spectrum which has spectral peaks at ω^- and ω^+ .

The resonance frequency of the anti-bonding and bonding mode can be calculated by comparing the coefficients of the following equation

$$(\omega - \tilde{\omega}_1)(\omega - \tilde{\omega}_2) + \kappa_{12}\kappa_{21} = (\omega - \tilde{\omega}^+)(\omega - \tilde{\omega}^-), \quad (3.7)$$

then we can derive a quadratic equation

$$(\tilde{\omega}^{+,-})^2 - (\tilde{\omega}_1 + \tilde{\omega}_2)\tilde{\omega}^{+,-} + (\tilde{\omega}_1\tilde{\omega}_2 + \kappa_{12}\kappa_{21}) = 0. \quad (3.8)$$

This gives the formal solutions to be found

$$\tilde{\omega}^{+,-} = \frac{\tilde{\omega}_1 + \tilde{\omega}_2}{2} \pm \sqrt{\left(\frac{\tilde{\omega}_1 - \tilde{\omega}_2}{2}\right)^2 - \kappa_{12}\kappa_{21}}. \quad (3.9)$$

Since the value of $\tilde{\omega}_1$, $\tilde{\omega}_2$ and also κ_{12} , κ_{21} are complex, the square root operation results in the formation of Riemann sheet in a complex plane.

Moreover, if we set δ as the difference between the resonance frequencies of two resonators and κ as the average of mutual coupling strength, we can make diagrams for the real and imaginary part of $\tilde{\omega}^+$ and $\tilde{\omega}^-$ in the parametric plane composed of δ and κ (see Figure 17).

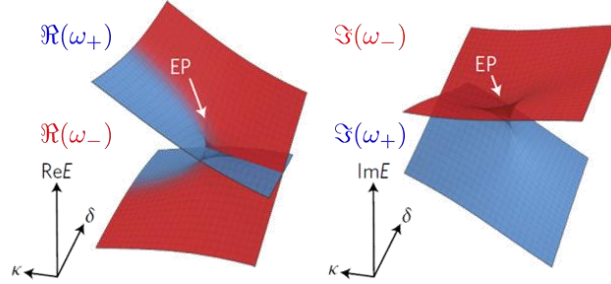


Figure 17 Diagrams for the real and imaginary part of the hybrid resonance frequencies $\tilde{\omega}^+$ and $\tilde{\omega}^-$ as a function of δ and κ

Both diagrams have a singular point at the same position, which is called exceptional point. Therefore, we can find the condition for the exceptional point

$$\left(\frac{\tilde{\omega}_1 - \tilde{\omega}_2}{2}\right)^2 = \kappa_{12}\kappa_{21}. \quad (3.10)$$

This confirms that the position of the exceptional point is directly related to the values of the mutual coupling constants. In the case of the Born-Kuhn model, its chiral nature is expected to cause different mutual coupling constant depending on the handedness of the incident circular polarization. In order to verify this, we conducted optical simulations for the Born-Kuhn model, and calculated the mutual coupling constants under the illumination of left- and right-handed circularly polarized light.

First, we constructed the Born-Kuhn model with two gold nano-bars.

The width, depth and thickness of the bars were 300 nm, 50 nm and 50 nm, respectively. They were orthogonally oriented and the upper bar was placed 60 nm above the lower one as shown in Figure 18 (a). For Left- and right-handed circularly polarized light normally incident on the structure, the complex extinction cross-sections were calculated by rigorous multipole method.⁴ The resulting extinction cross-sections then were fitted as a sum of rational fraction polynomials⁵

$$\tilde{a}(\omega) = \sum_n \frac{\tilde{a}_n}{\omega - \tilde{\omega}_n}. \quad (3.11)$$

The mutual coupling constants were calculated from the values of hybrid mode amplitudes and complex resonance frequencies³

$$\begin{aligned} \kappa_{12} &= \frac{\tilde{a}_1^+ \tilde{a}_1^-}{\tilde{a}_1^+ \tilde{a}_2^- - \tilde{a}_1^- \tilde{a}_2^+} (\tilde{\omega}^+ - \tilde{\omega}^-), \\ \kappa_{21} &= \frac{\tilde{a}_2^+ \tilde{a}_2^-}{\tilde{a}_1^+ \tilde{a}_2^- - \tilde{a}_1^- \tilde{a}_2^+} (\tilde{\omega}^+ - \tilde{\omega}^-). \end{aligned} \quad (3.12)$$

In Figure 18 (b), we observed distinct mutual coupling constants for left- and right-handed circularly polarized light, and the results revealed that the mutual coupling strength strongly depends on the circular polarization state.

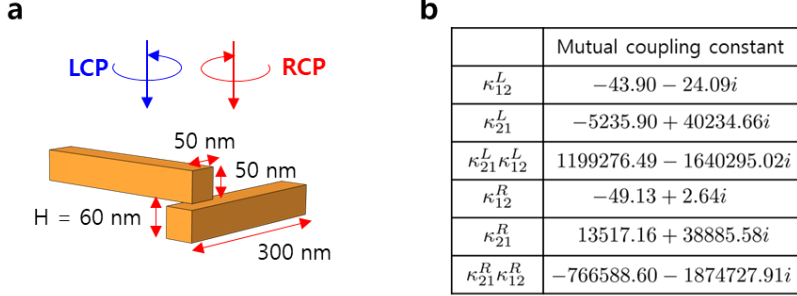


Figure 18 Optical simulation of the Born-Kuhn model. (a) Schematic showing the dimensions for the constructed Born-Kuhn model. (b) Calculated mutual coupling constants for left- and right-handed circular polarization.

Moreover, the validity of the simulation was confirmed by using parallelly coupled nano-rods which have achiral conformation. The width, depth and thickness of the rods were the same as the previous model. The lateral shift between the rods were 100 nm, and the upper rod is placed 60 nm above the lower one (see Figure 19 (a)). Likewise, we calculated the mutual coupling constants for both circularly polarization and found out that they were similar to each other (Figure 19 (b)). Therefore, we concluded that since the Born-Kuhn model has mutual chiral interaction which differently reacts to left- and right-handed circular polarization, the position of the exceptional point also depends on the circular polarization state.

However, we aware that our phenomenological approach has inherent limitations because it cannot support our theory without the simulation data, hence analytic approaches are needed to supplement the theory. Also, we have to consider more carefully if the coupled mode theory can be appropriately applied for this condition.⁶

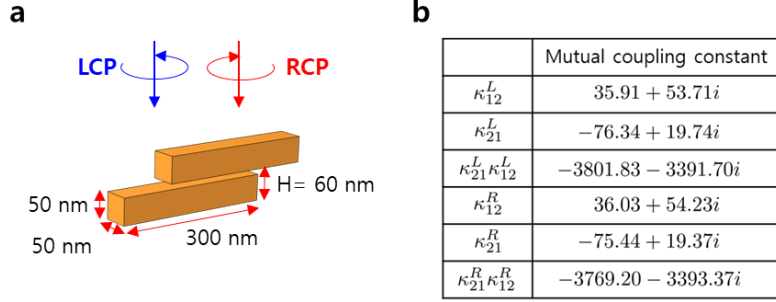


Figure 19 (a) Optical simulation of the parallelly coupled rods. (a) Schematic showing the dimensions for the constructed model of parallelly coupled rods. (b) Calculated mutual coupling constants for left- and right-handed circular polarization.

3.3 Numerical Demonstration of the Exceptional Point

In this section, numerical calculation has been conducted to substantiate the theoretical prediction discussed in Chapter 3.1. In order to demonstrate the exceptional point, we constructed the array structure of the Born-Kuhn model, and modulated the geometric parameters to generate the interference between two hybridized modes. Complex resonance frequency for each mode was obtained from the spectral analysis, and we drew EP diagrams for the real part (resonance frequency) and imaginary part (loss rate) of the complex resonance pulsation. The results indicates that there is clear difference in the position of the exceptional point for left- and right-handed circular polarization, which is consistent with the theoretical prediction.

A commercial software solving Maxwell's equations based on finite element method (COMSOL 5.6) has been used for the optical simulation. We modeled the periodic structures of the orthogonally aligned nanorods on a glass substrate (with refractive index of 1.45). A spacer (with refractive index of 1.5) was placed between the upper and lower rods to distinguish them in optically different environment. Light was coming from an air medium and normally incident on the structure, and we put perfectly matched layers (PML) on the top and the bottom of the simulation domain to absorb the residual field. To find the exceptional point of the Born-Kuhn model, two parameters were used for searching: the displacement between the upper and lower rod along x-direction d_x and the period along y-direction P_y . While setting the dimensions of the Born-Kuhn symmetry unit, several points needed to be considered. First, each nanorod should have an appropriate aspect ratio to exhibit sufficient optical responses to be analyzed. Second, the vertical distance between the upper and lower rods should be close to have distinguished hybridized resonance frequencies. Therefore, the geometry of the Born-Kuhn was set up as shown in

Figure 20 (c).

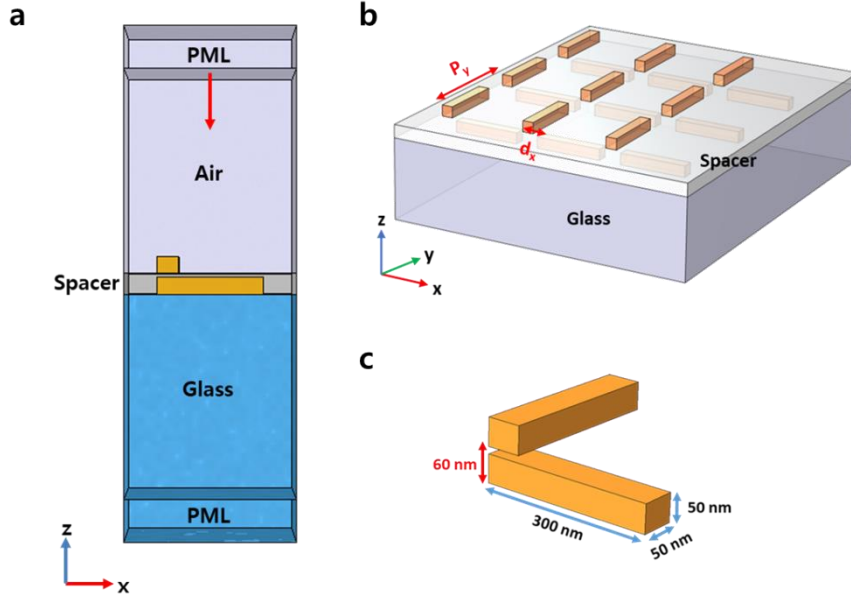


Figure 20 Optical simulation of the periodic Born-Kuhn model. (a) Schematic of the simulation setup. (b) Three-dimensional design for the periodic structure of the Born-Kuhn model. (c) The dimensions of the Born-Kuhn unit.

An input and output ports were installed on the top and bottom boundaries between PML layers, respectively. In the port boundary setting, the incident light came from the input port and the transmitted electric field \mathbf{E}_t was measured in the output port. We measured the transmission coefficients under the illumination of left- and right-handed circularly polarized light by the following S-parameter calculation,

$$S_{21} = \frac{\int_{\text{output port}} (\mathbf{E}_t \cdot \mathbf{E}_{out}^*) dA}{\int_{\text{output port}} (\mathbf{E}_{out} \cdot \mathbf{E}_{out}^*) dA}, \quad (3.13)$$

where \mathbf{E}_{out} was set to be the same as the incident polarization state. Then, the rational fitting of the complex transmission coefficient spectra gives,⁷

$$S_{21}(s) = \sum_{k=1}^n \frac{C_k}{s - A_k} + D, \text{ where } s = i * 2\pi f \quad (3.14)$$

and the resonance frequency f_R and the loss rate γ can be obtained from the poles A_k :

$$f_R = \frac{\Im(A_k)}{2\pi}, \quad \gamma = -\frac{\Re(A_k)}{\pi}. \quad (3.15)$$

The existence of the exceptional point was confirmed by examining the positions of the resonance frequencies and the loss rates of two hybrid modes with regard to the displacement d_x and the periodicity P_y . For instance, for $P_y = 490$ nm, we observed a crossing behavior of the resonance frequencies and an avoided crossing of the loss rates. However, for $P_y = 500$ nm, 510 nm, the opposite trends appeared: an avoided crossing of the resonance frequencies while a crossing of the loss rates were observed. This indicates that there is an exceptional point where both the resonance frequencies and loss rates of the hybrid modes coalesce.

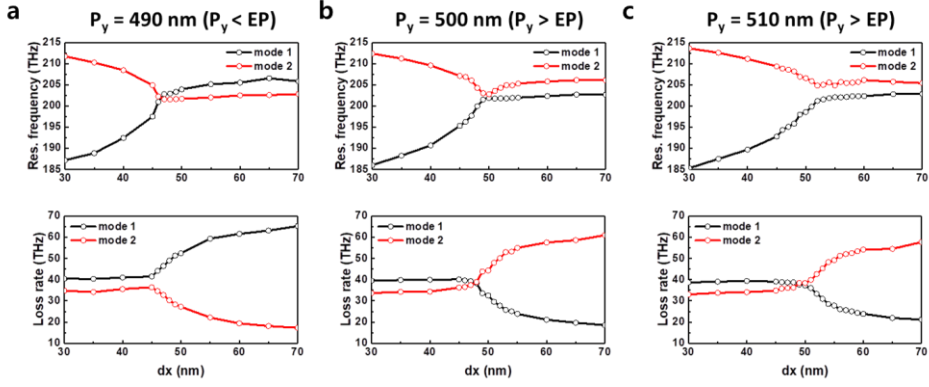


Figure 21 Resonance frequencies and loss rates under the illumination of left-handed circular polarized light as a function of d_x for (a) $P_y = 490$ nm, (b) $P_y = 500$ nm and (c) $P_y = 510$ nm

We can create surface plots for the resonance frequencies and loss rates as a function of d_x and P_y to visualize the interference between two eigenmodes more clearly. The surfaces of the hybrid modes were intertwined, and one singular point, which refers to the exceptional point, was observed. Also, we obtained distinct positions of the exceptional point depending on the handedness of circular polarization. The position was found be $d_x = 48$ nm and $P_y = 495$ nm for left-handed circularly polarized light, and $d_x = 51$ nm and $P_y = 505$ nm for right-handed circularly polarized light. This implies that the exceptional can be tuned by the circular polarization state of the incident beam, and the numerical results corroborate the theoretical prediction.

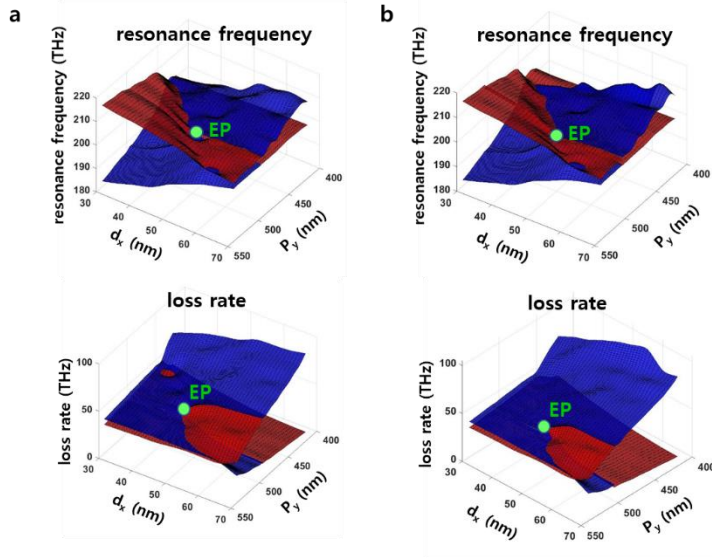


Figure 22 EP diagrams of the resonance frequencies and loss rates for (a) left-handed and (b) right-handed circular polarization

Based on the theoretical prediction and numerical results, we suggest a potential application of the non-Hermitian Born-Kuhn model utilizing the tunability of the exceptional point. For example, it can produce a topologically-driven design criteria for ultrasensitive chiral molecule sensing. If the structure is designed for having an exceptional point under LCP illumination, the optical state is not located at the exceptional point for RCP incidence since the exceptional point moved its position. Therefore, the system is more sensitive for LCP light when the perturbation is small.

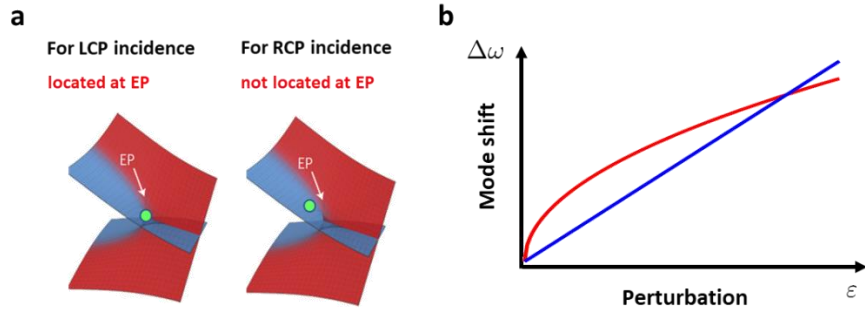


Figure 23 (a) Different EP diagrams for LCP and RCP incidence. (b) Different mode shift as a function of perturbation for LCP (red) and RCP (blue)

3.4 Bibliography

- (1) Haus, H. A.; Huang, W. Coupled-Mode Theory. **1991**, 1505–1518.
- (2) Bakhti, S.; Destouches, N.; Tishchenko, A. V. Analysis of Plasmon Resonances on a Metal Particle. *J. Quant. Spectrosc. Radiat. Transf.* **2014**, *146*, 113–122. <https://doi.org/10.1016/j.jqsrt.2014.01.014>.
- (3) Bakhti, S.; Destouches, N.; Tishchenko, A. V. Coupled Mode Modeling to Interpret Hybrid Modes and Fano Resonances in Plasmonic Systems. *ACS photonics* **2015**, *2* (2), 246–255.
- (4) Grahn, P.; Shevchenko, A.; Kaivola, M. Electromagnetic Multipole Theory for Optical Nanomaterials. *New J. Phys.* **2012**, *14*. <https://doi.org/10.1088/1367-2630/14/9/093033>.
- (5) Acuña, C. G. Rational Fraction Polynomial Method (<https://www.mathworks.com/matlabcentral/fileexchange/3805-rational-fraction-polynomial-method>), MATLAB Central File Exchange. Retrieved May 30, **2021**.
- (6) Joannopoulos, J. D.; Johnson, S. G.; Winn, J. N.; Meade, R. D. Molding the Flow of Light. *Princet. Univ. Press. Princeton, NJ [ua]* **2008**.
- (7) Gustavsen, B.; Semlyen, A. Rational Approximation of Frequency Domain Responses by Vector Fitting. *IEEE Trans. power Deliv.* **1999**, *14* (3), 1052–1061.

Chapter 4. Concluding Remarks

The notion of non-Hermitian physics and the exceptional point was first discussed within the field of quantum physics. However, the introduction of the concept in photonics resulted in an explosion of researches demonstrating novel features. Moreover, it was also introduced in the field of plasmonics, and a variety of research activities have been creating exotic applications. Still, for the implementation of the concept to chiral plasmonics, few attempts have been made. In this context, we developed a design principle for the demonstration of non-Hermitian chiral nanomaterials.

For the sake of simplicity, Born-Kuhn model, the simplest chiral model, was utilized as a chiral nanostructure, and its geometric parameters d_x and P_y were modulated to find an exceptional point. The real and imaginary part of the hybridized plasmon modes corresponds to the resonance frequency and loss rate, respectively, and they were obtained from the transmission coefficient data. We observed the resonance frequencies and loss rates of two hybrid modes being intertwined as a function of d_x and P_y , and found the exceptional point where both the real and imaginary parts coalesce. Strikingly, the Born-Kuhn model exhibits distinct exceptional points for left- and right-handed circularly polarized light.

We also developed a theoretical framework of analyzing the non-Hermitian system utilizing coupled mode theory. We added mutual coupling constant which determines the chirality of the Born-Kuhn model and predicted different position of exceptional point for left and right-handed circular polarization.

In conclusion, we found that the exceptional point of the Born-Kuhn

model can be tuned by the handedness of the circular polarization. We believe that the result can be generalized to chiral nanomaterials, and it has significant implication for the application of spin-controlled optical devices such as ultrasensitive chiral molecule sensing.

초 록

홀짝성-시간 대칭성의 발견은 비-허미시안 (non-Hermitian) 물리학 분야에서 큰 족적을 남겼다. 이는 양자역학의 ‘에너지의 양자화’의 개념을 재정의했을 뿐만 아니라 수리물리학의 범위를 실험물리학에서 복소 해석학으로 확장시켰다. 또한, 사람들은 양자역학의 슈뢰딩거 방정식과 전자기학의 맥스웰 방정식의 유사성을 확인하여 홀짝성-시간 대칭성의 개념을 광학에 적용시켰다.

이 비-허미시안 광학은 내재된 위상 기하적 특성과 특이점을 활용한 수많은 연구들을 창출시켰다. 더 나아가, 비-허미시안의 개념은 플라즈모닉스 분야에 적용되어 극도로 민감한 분자 센싱과 같은 새로운 분야를 만들어가고 있다. 최근 UC, Berkeley의 한 연구진은 커플링된 금 나노막대 배열을 제작해 플라즈모닉 시스템에서 특이점을 구현하는 데에 성공했다. 그들은 나노막대 사이의 x-방향 거리와 y-방향의 주기적 거리를 조절하여 근접장과 원거리장의 커플링을 제어하였고, 혼성화된 모드의 간섭을 일으켜 특이점을 구현하였다. 또한, 기존의 센서 성능과의 비교를 통해 더 낮은 농도에서 높은 민감도를 가짐을 확인하였다.

비-허미시안 플라즈모닉스 분야의 연구들을 기반으로 우리는 비-허미시안 물리학에 대한 이해를 카이럴 플라즈모닉스 분야로 확장시키는 것에 초점을 맞췄다. 카이럴 플라즈모닉스 물질은 빛의 원형편광의 방향에 따라 광학적 특성이 달라지는 카이럴 광학 특성을 가지고 있고, 이를 통해 여러가지 광학 분야에 활용되고 있다. 최근 본 연구진은 용액 공

정 기반의 카이럴 플라즈모닉 나노입자 합성을 보고한 바 있다. 합성된 나노입자는 갭 (gap) 구조체에서 전기 쌍극자와 자기 쌍극자가 서로 얹혀 큰 광학 활성도를 갖게 된다. 이러한 광학적 특성을 활용한다면 비-허미시안 카이럴 나노입자 시스템의 구현은 카이럴 플라즈모닉스 분야에서 큰 족적을 남길 것이라 기대된다.

그러나 카이럴 나노입자의 복잡한 광학적 특성은 체계적인 분석을 저해하여 본 연구에서는 카이럴 현상을 설명할 수 있는 가장 간단한 모델인 Born-Kuhn model를 이용하였다. Born-Kuhn model은 서로 수직으로 배열된 두 개의 나노막대로 이루어진 모델로써 기하학적 특성을 조절하기 용이하기 때문에 비-허미시안 카이럴 플라즈모닉 현상을 분석하기 위한 좋은 도구로 작용했다. 이를 통해, 본 연구에서는 이론적 접근과 수치해석적인 접근 방법을 통해 Born-Kuhn model의 특이점 구현을 진행하였다.

이론적인 방법론으로는 커플링된 플라즈몬 모드를 설명하기 위해 coupled mode 이론이 사용되었다. Born-Kuhn model의 카이럴한 상호작용을 표현하기 위해 상호 커플링 상수를 도입하였고, 좌회전편광과 우회전편광에 대해서 상이한 특이점이 관찰될 것임을 예측했다. 이를 뒷받침하고자 수치해석적인 방법을 이용하였고, 이를 위해 유한 요소 기법으로 맥스웰 방정식의 해를 구하는 상용 소프트웨어인 COMSOL을 활용했다. Born-Kuhn model에서 상호 간의 거리와 주기적 배열을 조절하여 혼성화 모드의 위치를 계산했고, 이론적 예측과 동일하게 좌회전편광과 우회전편광에 대해 다른 특이점이 관찰되었다.

본 결과는 비-허미시안 Born-Kuhn model이 극도로 민감한 카이럴 분자 센싱에 활용될 수 있음을 시사했다. 섭동 이론에 따르면, 시스템이 특

이점 위에 놓여있게 되면 외부 자극에 대해 선형적으로 반응하는 것이 아닌 제곱근에 비례하여 반응하게 된다. 따라서 만약, 좌회전편광을 입사시켰을 때 시스템이 특이점 위에 있게 된다면, 우회전편광보다 좌회전편광에서 더 민감하게 반응하게 되는 것이다. 우리는 이러한 회전편광에 대한 민감도의 차이를 이용해 카이럴 분자 센싱에 활용할 수 있다.

본 학위 연구에서는 비-허미시안 광학에서 카이럴 나노물질의 광학적 작용을 근본적으로 이해하기 위한 연구를 진행했다. 이를 통해, 비-허미시안 카이럴 플라즈모닉 공진기의 광학적 특징에 대한 기초적인 이론을 정립하였다. 더 나아가, 빛의 스핀에 따라 특이점이 조절되는 시스템의 구현은 카이럴 분자의 센싱 분야에서 새로운 방법론을 제시해줄 것이라 기대된다.

주요어: 비-허미시안 물리학, 홀짝성-시간 대칭성, 특이점, 카이럴 플라즈모닉스, coupled mode 이론

학번: 2019-24094